

# Solid-State NMR and MRI Spectroscopy for Li/Na Batteries: Materials, Interface, and In Situ Characterization

Xiangsi Liu, Ziteng Liang, Yuxuan Xiang, Min Lin, Qi Li, Zigeng Liu, Guiming Zhong, Riqiang Fu, and Yong Yang\*

Enhancing the electrochemical performance of batteries, including the lifespan, energy, and power densities, is an everlasting quest for the rechargeable battery community. However, the dynamic and coupled (electro)chemical processes that occur in the electrode materials as well as at the electrode/electrolyte interfaces complicate the investigation of their working and decay mechanisms. Herein, the recent developments and applications of solid-state nuclear magnetic resonance (ssNMR) and magnetic resonance imaging (MRI) techniques in Li/Na batteries are reviewed. Several typical cases including the applications of NMR spectroscopy for the investigation of the pristine structure and the dynamic structural evolution of materials are first emphasized. The NMR applications in analyzing the solid electrolyte interfaces (SEI) on the electrode are further concluded, involving the identification of SEI components and investigation of ionic motion through the interfaces. Beyond, the new development of in situ NMR and MRI techniques are highlighted, including their advantages, challenges, applications and the design principle of in situ cell. In the end, a prospect about how to use ssNMR in battery research from the perspectives of materials, interface, and in situ NMR, aiming at obtaining deeper insight of batteries with the assistance of ssNMR is represented.

## 1. Introduction

Electric vehicles (EVs) and artificial intelligence (AI) equipment gradually become indispensable parts of our contemporary life. The further development of their longevity is inseparable from the innovation of energy storage equipment.<sup>[1]</sup> Lithium ion batteries (LIBs) are the leading energy storage technology among various kinds of secondary batteries due to their advantages in high energy density, non-memory effect, and long cycle stability.<sup>[2]</sup> To meet the requirements of sustainable development of large-scale energy storage facilities such as low cost and non-toxic, sodium ion batteries (NIBs), analogous to LIBs, have also received a great attention in recent years.<sup>[3]</sup> How to develop energy storage materials with high performance involves not only the design and preparation of electrode materials, but also the fundamental research such as the structure analysis, ionic/electronic transport characteristics, multiple (electro)chemical and phase transition processes during

the charge-discharge cycles of batteries. Thus the in-depth understanding of structure-performance relationship and electrochemical reaction mechanism of the battery materials can provide a comprehensive theoretical and experimental guidance and thereafter continuous improvement of batteries.

Most of the components inside secondary batteries are solid state except for the liquid electrolyte, which can also be replaced by solid-state electrolytes (SSEs) to improve the energy density and safety of secondary batteries currently.<sup>[4]</sup> Therefore, advanced characterization techniques suitable for detecting solid-state materials are essential for diagnosing the secondary batteries.<sup>[5]</sup> Complementary to the long-range diffraction methods, solid-state nuclear magnetic resonance (ssNMR) is a powerful tool to probe the local environment of atoms/ions both in crystalline and amorphous materials, and has unique advantages in revealing the electrochemical reaction mechanism and microscopic ionic dynamics.<sup>[6]</sup> The methods for characterizing the short-range structure of materials mainly include X-ray absorption spectroscopy (XAS), Pair Distribution Function (PDF) and ssNMR techniques. The laboratory-scale ssNMR technique shows experimental convenience as compared to XAS and PDF techniques that require synchrotron


X. Liu, Z. Liang, Y. Xiang, M. Lin, Dr. Q. Li, Prof. Y. Yang  
State Key Laboratory for Physical Chemistry of Solid Surfaces  
Department of Chemistry  
College of Chemistry and Chemical Engineering  
Xiamen University  
Xiamen 361005, P. R. China  
E-mail: yyang@xmu.edu.cn

Dr. Z. Liu  
Forschungszentrum Jülich  
IEK-9, 52425 Jülich, Germany

Dr. G. Zhong  
Xiamen Institute of Rare Earth Materials  
Chinese Academy of Sciences  
Xiamen 361021, P. R. China

Dr. R. Fu  
National High Magnetic Field Laboratory  
1800 E. Paul Dirac Drive, Tallahassee, FL 32310, USA

Prof. Y. Yang  
College of Energy  
Xiamen University  
Xiamen 361005, P. R. China

 The ORCID identification number(s) for the author(s) of this article can be found under <https://doi.org/10.1002/adma.202005878>.

DOI: 10.1002/adma.202005878

radiation sources. Furthermore, the abundant NMR-active nuclei cover the most of constituent elements of battery's materials, which brings highly compatibility between ssNMR and battery technologies. Especially,  ${}^6\text{Li}$  and  ${}^{23}\text{Na}$  as the charge carriers, directly participate in the electrochemical processes of LIBs and NIBs, respectively, and become the most frequently probed atoms in the field of energy storage technologies.<sup>[7]</sup> Moreover, the skeletal atoms, including  ${}^{19}\text{F}$ ,  ${}^{17}\text{O}$ ,  ${}^{31}\text{P}$ ,  ${}^{33}\text{S}$ , etc., can also provide important information regarding the structural and electronic properties. Furthermore, beyond the LIBs and NIBs systems,  ${}^{25}\text{Mg}$ ,  ${}^{27}\text{Al}$ ,  ${}^{39}\text{K}$ ,  ${}^{43}\text{Ca}$ , and  ${}^{67}\text{Zn}$  are also used in various energy storage systems, such as magnesium ion batteries, potassium ion batteries, etc.<sup>[6a,8]</sup>

Different from the random and rapid thermal motion (the tumbling rate  $\approx 10^9\text{--}10^{12}$  Hz) in liquid samples, which is much larger than the frequency range of anisotropic effects such as chemical shift and dipole coupling, the molecular motion is rather limited in the solid samples. Therefore, the dipole-dipole and anisotropic interactions in solid materials cannot be effectively averaged out as in solution sample.<sup>[9]</sup> Fortunately, the operating mechanism of batteries is based on electron transfer reaction. The unpaired electrons and conductive electrons exist in electrode materials and/or their electrochemical cycling process, and are contributed to Fermi-contact interaction and Knight shift respectively. These shift-mechanisms induce very different chemical shift for various components of batteries thus spreading the signals over a large range. Taking LCO||Li battery as an example, the  ${}^7\text{Li}$  chemical shift of LCO is in the range of 0–100 ppm depending on the charge state. While the signal of Li metal centers at 250 ppm and that of electrolyte and SEI species appears at around 0 ppm. Therefore, ssNMR is capable of characterizing each component. In addition to the chemical shift, some of interactions are also related to the ionic motion. For instance, the fast ionic motion can average dipole–dipole interaction, thus contributing to a narrow line-width of NMR signal and leading to different responses on the NMR relaxation properties. Therefore, complemented with advanced NMR methods and pulse sequences (Table 1), ssNMR technique can provide fruitful information on the kinetics of target nucleus transport in the material by measuring the spin-lattice relaxation time ( $T_1$ ) and the spin-spin relaxation time ( $T_2$ ), especially with two-dimensional exchange spectroscopy (2D-EXSY), pulsed-field gradient (PFG), and variable-temperature (VT) experiments, the ionic transport between the different sites, the ions self-diffusion coefficient, and the transition activation energy can be unraveled.<sup>[10]</sup> Moreover, in situ NMR technique has been developed to detect the air-sensitive, unstable, and short-lived intermediate products during cycling, revealing the real time reaction mechanism inside the batteries.<sup>[11]</sup>

The basic operation processes of ssNMR and in situ experiments,<sup>[6a]</sup> the characteristics of in situ NMR experiment<sup>[12]</sup> and the applications of ssNMR in the functional nanomaterials<sup>[9b]</sup> could be found in the literatures. In this progress report, different research recipes from our and other groups over the past few years are selected to illuminate the applications of ssNMR and MRI in LIBs and NIBs. Given that the electrochemical performance of the battery greatly depends on the battery material, unraveling the dynamic

**Table 1.** NMR methods and corresponding applications in materials for LIBs and NIBs.

NMR methods	Applications in materials for LIBs/NIBs	Ref.
Magic-angle spinning, MAS	Suppressing dipole interactions and anisotropic interactions to obtain high-resolution spectra.	[14]
Relaxation times, $T_1/T_2$	Acquisition of ionic mobility information.	[28]
Variable temperature, VT	Acquisition of ionic mobility information.	[29]
Spin-echo mapping	Obtaining quantitative information with a broad spectrum.	[30]
Hahn-echo	Baseline correction and measurement of $T_2$ .	[31]
Rotational echo double resonance, REDOR	Measuring distance between two different nuclei.	[22]
Projection of magic-angle turning phase-adjusted spinning sidebands, pj-MATPASS	Separation of the isotropic and anisotropic resonances and suppression of sidebands.	[16]
Cross polarization, CP	Increase the peak intensity of the nucleus with low gyromagnetic and natural abundance and reducing the experimental collection time.	[32]
Exchange spectroscopy, EXSY	Acquisition of ionic transport path and self-diffusion coefficient.	[33]
Pulsed-field gradient, PFG	Acquisition of the self-diffusion coefficient and performing MRI.	[32]
Dynamic Nuclear Polarization, DNP	Significantly increase the sensitivity of NMR to reduce the time of spectrum acquisition, especially for the interface characterization.	[34]
In situ NMR	Acquisition of the metastable structure produced during the electrochemical reaction.	[35]
Magnetic resonance Imaging, MRI	Observation and determination of the distribution of probe nucleus in the sample.	[32,36]

material structural evolution and the electrochemical reaction mechanism can better guide the design and development of materials for practical applications. In addition, the SEI layer on the electrodes profoundly affects the rate performance and cycle stability of battery. On the other hand, in situ NMR technique is essential to reveal unstable mesophases and dynamic structural changes during cycling. Therefore, we focus on these three most important aspects: electrode/electrolyte materials, SEI and in situ NMR (Figure 1). A perspective on future developments are also given at the end. We hope these examples can provide the readers with new ideas from the perspective of ssNMR when encountering similar challenges in their research work.

## 2. Materials Characterization

This section highlights the outstanding advantages of ssNMR in characterizing and tracking the local structural environment of some LIBs/NIBs materials during the electrochemical cycling. Besides, the first-principles calculations of chemical shift of paramagnetic materials are reviewed in Section 2.3.

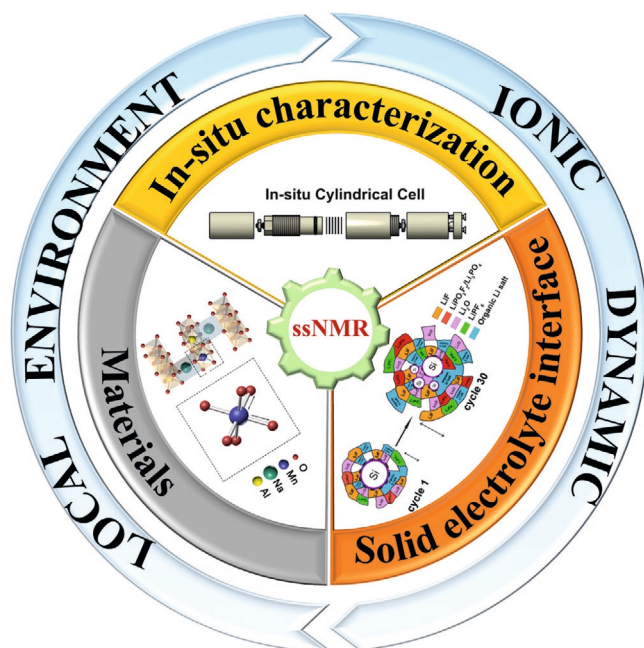


**Figure 1.** The main research scope of the applications of ssNMR for LIBs and NIBs chemistries.

## 2.1. Confirmation of the Composition and Structure for Pristine Materials

As a basic function of ssNMR, the chemical composition of the materials can be obtained by using multiple nuclei probes for co-verification. SSEs are considered to inherently improve the safety and energy density of batteries.<sup>[13]</sup> Among various types of SSEs, the sulfide SSE exhibits the highest ionic conductivity close to that of liquid electrolytes but is unstable even in the conventional ball-milling process.<sup>[14]</sup> As shown in  ${}^6\text{Li}$ ,  ${}^{31}\text{P}$ , and  ${}^{119}\text{Sn}$  MAS NMR spectra of  $\text{Li}_{10}\text{SnP}_2\text{S}_{12}$  before and after ball-milling (Figure 2a),  $\text{Li}_{10}\text{SnP}_2\text{S}_{12}$  would decompose into  $\text{Li}_3\text{PS}_4$  (84 ppm in  ${}^{31}\text{P}$  NMR) and  $\text{Li}_4\text{SnS}_4$  ( $\approx 50$  ppm in  ${}^{119}\text{Sn}$  NMR) due to the high mechanical and thermal energy during ball-milling process, therefore a more gentle mixing process is necessary for the preparation of composite electrodes for all solid-state sulfide batteries, otherwise the assembled all-solid-state batteries (ASSBs) would exhibit obvious voltage polarization and thus low initial capacity.<sup>[14]</sup>

Identifying the locations of ions in the electrode/electrolyte materials is a key topic for the structure confirmation and understanding the ionic transport mechanism. For example, Wang et al. used the differences in  $T_1$  to selectively suppress the strong signals from the octahedral site 48g (shorter  $T_1$ ,  $\approx 1.9$  ppm) and thus to successfully reveal the additional site of distorted octahedral 96h (longer  $T_1$ ,  $\approx 1.6$  ppm) in  $\text{Li}_{7-2x-3y}\text{Al}_y\text{La}_3\text{Zr}_{2-x}\text{W}_x\text{O}_{12}$  by using high-resolution  ${}^6\text{Li}$  ssNMR. Furthermore, the average  $\text{Li}^+$  diffusion coefficient on the order of  $10^{-12}$   $\text{m}^2 \text{ s}^{-1}$  was obtained by fitting  ${}^7\text{Li}$  PFG NMR spectra at variable temperature. The shorter  $T_1$  of 48g site than that of 96h and 24d ( $\approx 0.8$  ppm) sites indicates that the  $\text{Li}^+$  ions on the 96h and 24d sites diffuse rather slowly.<sup>[15]</sup> Most of the cathode materials can be classified as paramagnetic materials due to

the presence of 3d/4d transition metal (TM) ions with unpaired electrons. Therefore, the unpaired electron spin density is transferred from paramagnetic TM ions to the nucleus under observation, resulting in wide and overlapping resonances. Benefited from the development of magic angle spinning (MAS) NMR technique and advanced pulse methods (Table 1), such as the projection of magic-angle turning phase-adjusted spinning sidebands (pj-MATPASS) sequence,<sup>[16]</sup> the anisotropic interactions and the spinning sidebands could be effectively suppressed to acquire high resolution spectra for cathode materials. Ternary materials ( $\text{LiNi}_x\text{Co}_y\text{Mn}_{1-x-y}\text{O}_2$ ,  $\text{LiNi}_x\text{Co}_y\text{Al}_{1-x-y}\text{O}_2$ ) show great prospects in field of electric vehicles, but the arrangement of multiple metal elements makes their structure difficult to unravel. Through high-resolution  ${}^6\text{Li}$  MAS NMR, Yoon et al. provided the presence of  $\text{Li}^+$  in the TM layers of  $\text{LiCo}_{1/3}\text{Ni}_{1/3}\text{Mn}_{1/3}\text{O}_2$  because the  $\text{Li}^+$  ions in TM layers are subjected to greater Fermi-contact interactions than that in the  $\text{Li}^+$  layers.<sup>[17]</sup> With further combining  ${}^6\text{Li}$  MAS NMR with Reverse Monte Carlo (RMC) calculations, Zeng et al. proposed that  $\text{Ni}^{2+}$  and  $\text{Mn}^{4+}$  tend to exist in the TM layers in the form of clusters rather than a random distribution.<sup>[18]</sup> Zheng et al. found that the peaks in the  ${}^7\text{Li}$  pj-MATPASS NMR spectra from the  $\text{Li}^+$ -doped  $\text{O3-NaLi}_{0.1}\text{Ni}_{0.35}\text{Mn}_{0.55}\text{O}_2$  sample could be divided into two groups, corresponding to chemical shifts above 1200 ppm (the  $\text{Li}^+$  in TM layers) and below 1200 ppm (the  $\text{Li}^+$  in the  $\text{Na}^+$  layers), and the  $\text{Li}^+$  in the TM layers could migrate into the Li layer at high voltage to suppress the structural change, leading to the long cycle stability.<sup>[19]</sup> After that, the theoretical calculation results of the Grey's group further support that the  ${}^7\text{Li}$  signals at the high and low chemical shifts correspond to  $\text{Li}^+$  in the TM layers and the Na layers, respectively (Figure 2b).<sup>[20]</sup>

Based on both TM ions and anions participating in the charge compensation during cycling, Li-excess materials can achieve a higher capacity than their theoretical value.<sup>[23]</sup> Directly probing the O local environments in these material systems is essential in order to gain a deeper understanding of the O redox behavior. However, the large quadrupole moment ( $I = 5/2$ ) and the low natural abundance of  ${}^{17}\text{O}$  nucleus make it difficult to get a high-resolution NMR spectrum, let alone directly connecting to the paramagnetic TM ions in the cathode materials. Through  ${}^{17}\text{O}$  enrichment, Grey's group first used  ${}^{17}\text{O}$  MAS ssNMR to explore the O environment of  $\text{Li}_2\text{MnO}_3$  material (Figure 2c).<sup>[21]</sup> Their results show that the two most intense peaks at 1859 and 2231 ppm should be assigned to the 4i and 8j sites, respectively, while the additional peaks are related to the stacking faults along c axis and the percentage of the stacking faults is  $\approx 10\%$  basing on the ratio of the intensities of the different  ${}^{17}\text{O}$  resonances. After that,  $\text{Li}_2\text{RuO}_3$  was further selected as a model material of 4d-TM Li-excess material to study oxygen local structure at both room temperature and high temperature.<sup>[24]</sup> More recently, House et al. first observed the formation of molecular  $\text{O}_2$  trapping in the bulk of  $\text{Li}_{1.2}\text{Ni}_{0.13}\text{Co}_{0.13}\text{Mn}_{0.54}\text{O}_2$  material with the chemical shift at  $\approx 3000$  ppm in the  ${}^{17}\text{O}$  NMR spectrum. Thus, they proposed that the large voltage hysteresis is associated with the loss of honeycomb superstructure.<sup>[25]</sup> However, the systematic study about the interpretation of the  ${}^{17}\text{O}$  local environment evolutions during anions redox process is still blank. In recent years, dynamic nuclear polarization (DNP) technique also shows the strength in enhancing



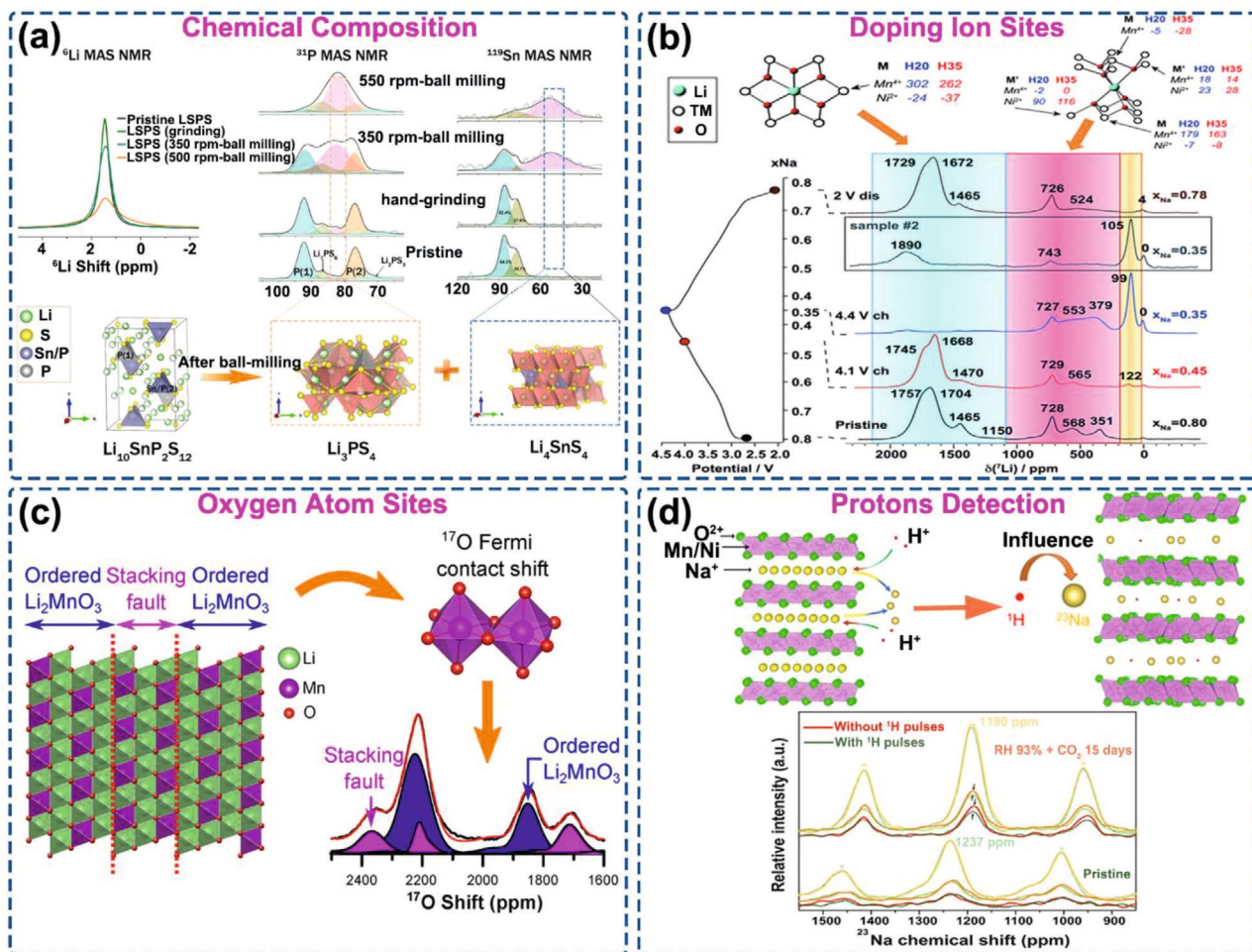


**Figure 2.** Confirmation of the composition and structure. a)  ${}^6\text{Li}$ ,  ${}^{31}\text{P}$ , and  ${}^{119}\text{Sn}$  MAS NMR spectra of the  $\text{Li}_{10}\text{SnP}_2\text{S}_{12}$  powder before and after different treatments. Reproduced with permission.<sup>[14]</sup> Copyright 2020, Elsevier. b)  ${}^7\text{Li}$  p-j-MATPASS NMR spectra of  $\text{P2-Na}_{0.8}\text{Li}_{0.12}\text{Ni}_{0.22}\text{Mn}_{0.66}\text{O}_2$ . Reproduced with permission.<sup>[20]</sup> Copyright 2017, Royal Society of Chemistry. c) Schematic representations of stacking faults and  ${}^{17}\text{O}$  MAS NMR spectrum of  ${}^{17}\text{O}$ -enriched  $\text{Li}_2\text{MnO}_3$ . Reproduced with permission.<sup>[21]</sup> Copyright 2016, American Chemical Society. d)  ${}^{23}\text{Na}\{^1\text{H}\}$  REDOR-dephased  ${}^{23}\text{Na}$  MAS NMR spectra of  $\text{Na}_{0.67}\text{Ni}_{0.33}\text{Mn}_{0.67}\text{O}_2$  powder exposed a relative humidity of 93% +  $\text{CO}_2$  atmosphere. Reproduced with permission.<sup>[22]</sup> Copyright 2020, Nature Research.

the sensitivity of low abundance nuclei in the bulk of micron sized materials,<sup>[26]</sup> especially for  ${}^6\text{Li}$  and  ${}^{17}\text{O}$ . Chakrabarty et al. proposed that a trace amount of paramagnetic ions ( $\text{Mn}^{2+}$  and  $\text{Gd}^{3+}$ ) doping can significantly boost the  ${}^7\text{Li}$  NMR signal in the bulk of  $\text{Li}_4\text{Ti}_5\text{O}_{12}$ .<sup>[26a]</sup> After that, they further extended this method to detect the  ${}^6\text{Li}$  and  ${}^{17}\text{O}$  signal. The signal enhancement factors of 142 was obtained for  ${}^6\text{Li}$  and the natural abundance  ${}^{17}\text{O}$  signals were detected.<sup>[26c]</sup> However, the paramagnetic dopants would change the initial structure of detected materials and the application of this method on Li-rich materials still needs to be studied.

Since its XRD patterns would not show obvious changes even after a long period of storage or immersion in water,  $\text{P2-Na}_{0.67}\text{Ni}_{0.33}\text{Mn}_{0.67}\text{O}_2$  has been considered as one of the most air-stable electrode materials. However, Grey's group found a new signal at 250–400 ppm appearing in  ${}^{23}\text{Na}$  MAS NMR spectrum when this material was charged above 3.7 V and their calculation results further proved that this additional signal

is attributable to the water molecules intercalating within the Na layers.<sup>[20]</sup> More recently, Yang's group performed the  ${}^{23}\text{Na}\{^1\text{H}\}$  rotational echo double resonance (REDOR) NMR to probe whether or not  $\text{H}^+$  and  $\text{H}_2\text{O}$  exist in the  $\text{Na}^+$  layers of pristine  $\text{Na}_{0.67}\text{Ni}_{0.33}\text{Mn}_{0.67}\text{O}_2$  material after being exposed in the extreme atmosphere of relative humidity 93% and the presence of  $\text{CO}_2$ . The lack of characteristic signal of hydration below 500 ppm proves that  $\text{H}_2\text{O}$  would not insert into  $\text{Na}^+$  layers. However, as shown in Figure 2d, the intensity of signal in the  ${}^{23}\text{Na}\{^1\text{H}\}$  REDOR NMR spectra for the exposed  $\text{Na}_{0.67}\text{Ni}_{0.33}\text{Mn}_{0.67}\text{O}_2$  sample decreases with the presence of  ${}^1\text{H}$  irradiation, as compared to that of pristine  $\text{Na}_{0.67}\text{Ni}_{0.33}\text{Mn}_{0.67}\text{O}_2$  sample, confirming that  $\text{H}^+$  ions are indeed exchanged into the structure of the exposed  $\text{Na}_{0.67}\text{Ni}_{0.33}\text{Mn}_{0.67}\text{O}_2$  sample with the extraction of  $\text{Na}^+$ , leading to poor electrochemical performance. Indeed, the  $\text{H}^+$ - $\text{Na}^+$  exchange mechanism is further confirmed through the electrochemical tests that the initial charge capacity of exposed- $\text{Na}_{0.67}\text{Ni}_{0.33}\text{Mn}_{0.67}\text{O}_2$  is lower than

that of pristine  $\text{Na}_{0.67}\text{Ni}_{0.33}\text{Mn}_{0.67}\text{O}_2$ . In contrast, for the Li-excess material, Wu and coworkers show that the introduction of  $\text{H}^+$  would lead to an unprecedented high initial Columbic efficiency for  $\text{Li}_2\text{MnO}_3$  electrode based on  $^2\text{H}$  MAS NMR and electrochemical results.<sup>[27]</sup> The above research examples indicate that ssNMR has become an important research method for qualitatively and quantitatively probing the chemical composition, atomic sites and structural defects in the solid-state materials. These results provide valuable experimental information for systematically understanding the structure-properties relationship.

## 2.2. Local Structural Evolution of Battery Materials during Charging–Discharging

Since ssNMR technique is sensitive to the microstructure, the qualitative and quantitative information on the short-range, and electronic structure of the sample can be extracted through analyses of the line shape, line intensity and chemical shift of the NMR signal, providing important basis for theoretical analysis and useful guidance for the development of existing materials and the design of new materials. In the following paragraphs, the application examples about the local structural evolution of cathode and anode materials during electrochemical reaction are introduced.

### 2.2.1. Lithium Cobalt Oxide

Due to the highest volume energy density and the outstanding cycling performance,  $\text{LiCoO}_2$  (LCO) materials have dominated the field of consumer electronics markets for more than 30 years. The local environment changes of lithium and cobalt atoms in LCO electrode have been investigated by  $^6\text{Li}$  and  $^{59}\text{Co}$  MAS NMR.<sup>[37]</sup>  $^7\text{Li}$  NMR signal exists at 0 ppm for the pristine LCO material because of the diamagnetic environment of  $\text{Li}^+$ . During the charging process, the  $\text{Li}^+$  signal would move away from 0 ppm because the increase of material conductivity and the Knight shift become dominant. The phase transitions information of the material can be obtained through the analysis of line shape and chemical shift. Hu's group reported the use of  $^{17}\text{O}$  MAS NMR to monitor the evolution of O local environment of pristine LCO during the first cycle and proposed that the  $^{17}\text{O}$  spectrum can reflect the phase changes since the O atoms serve as structural skeleton of the LCO materials.<sup>[37c]</sup> The single  $^{17}\text{O}$  signal at  $-636$  ppm was attributed to the diamagnetic environment in hexagonal O3 phases LCO ( $1 \geq x \geq 0.56$ ). In the delithiation process, this peak intensity decreases continuously and disappears at  $x = 0.5$  with the emerging of a new resonance at  $\approx 900$  ppm, corresponding to the phase transition between the hexagonal phase and the monoclinic phase. With further delithiation to  $x = 0.18$ , another signal appears at 1250 ppm corresponding to H1-3 phase and this signal would disappear completely when O1 phase  $\text{CoO}_2$  appears at  $x = 0.07$ .<sup>[37c]</sup> There are few studies about the influence of aliovalent doping on the local environment in the process of (de) lithiation for LCO. More recently, Wan et al. have systematically studied the structure evolution of the Al doping and Al/La

co-doping LCO electrodes through  $^6\text{Li}/^{59}\text{Co}$  MAS NMR, in situ XRD and XPS measurements.<sup>[38]</sup> Their  $^7\text{Li}$  NMR results showed that undoped LCO only has one narrow single phase at positive shift during charge process while Al-LCO and Al/La-LCO displays a distinctly asymmetrical peak, indicating that Al/La co-doping would induce more local structural phase and more continuous phase evolution than single Al doping LCO sample, and much more than the undoped LCO sample during cycling, which postpones the appearance of H1-3 phase and alleviates the volume change at high-voltage above 4.2 V.

### 2.2.2. Ternary Layered Oxides

When a part of Co atoms in the LCO is replaced with Ni/Mn or Ni/Al, the ternary layered oxides materials can be obtained, that is,  $\text{LiNi}_x\text{Co}_{1-x-y}\text{Mn}_y\text{O}_2$  (NCM) and  $\text{LiNi}_x\text{Co}_{1-x-y}\text{Al}_y\text{O}_2$  (NCA) materials, which exhibit higher energy density based on the redox reactions of  $\text{Ni}^{4+}/\text{Ni}^{2+}$ . The introduction of paramagnetic TM ions ( $\text{Ni}^{2+}$ ,  $\text{Ni}^{3+}$ , and  $\text{Mn}^{4+}$ ) in these materials and the various arrangement of TM ions near  $\text{Li}^+$  ions lead to a broad signal in the  $^{7/6}\text{Li}$  NMR spectra.<sup>[29,39]</sup> Nevertheless, combining in situ XRD and ssNMR together, Yang's group proposed that the phase transition process of the NCM material is closely related to the  $\text{Li}^+$  occupancy in the layered structure. As shown in **Figure 3a**, the major broad peak at 1100–250 ppm can be divided into two parts, at higher and lower than 700 ppm, corresponding to Li predominantly surrounded by  $\text{Mn}^{4+}$  ( $\text{Li}_M$ ) and  $\text{Ni}^{2+/3+}$  ions ( $\text{Li}_N$ ), respectively. Upon charging,  $\text{Li}_M$  is first extracted from the bulk and the range of this process is consistent with the existence of H1 phase. With the emerging of H2 phase, the signal shifts to a lower chemical due to the expansion of lattice parameter  $c$  and the oxidation of Ni ions. Afterward, a new group of shoulder peaks at around 750–300 ppm appear, corresponding to a newly formed H3 phase with a drastic decrease of lattice parameter  $c$ . At the end of delithiation process, an in-plane  $\text{Li}^+$  ordering process possibly occurs and  $\text{Li}^+$  might be distributed randomly in Li layer. In addition, the change of  $\text{Li}^+$  ions mobility of ternary materials during (de) lithiation can be obtained through VT ssNMR experiments and theoretical calculations.<sup>[29,39b]</sup> Accordingly, Grey's group proposed that  $\text{Li}^+$  hopping rate is accelerated from  $\approx 20\%$  state of charge (SOC) and reaches a maximum between 40% and 50% SOC because of the extending of  $\text{Li}^+$  vacancies and the layer spacing of NCM811 material. When the SOC reaches  $\approx 70\%$ , the overall layer spacing collapses rapidly, leading to decreased Li mobility.<sup>[29]</sup>

### 2.2.3. Organic Compound Materials

Organic compounds are deemed as the promising materials for the next-generation LIBs/NIBs because of their tunable molecular structure, recyclable and cost-efficient properties. ssNMR is very suitable for probing the initial structure,<sup>[41]</sup> the guest ions storage<sup>[40,41c,42]</sup> and ions transport mechanism<sup>[43]</sup> of organic materials, even part of them are amorphous. For example, Kai et al. used  $^{13}\text{C}$  MAS NMR to verify that 2,5-dichloro-3,6-dihydroxy-p-quinone (CLA) and  $\text{Na}_2\text{S}$  can effectively form



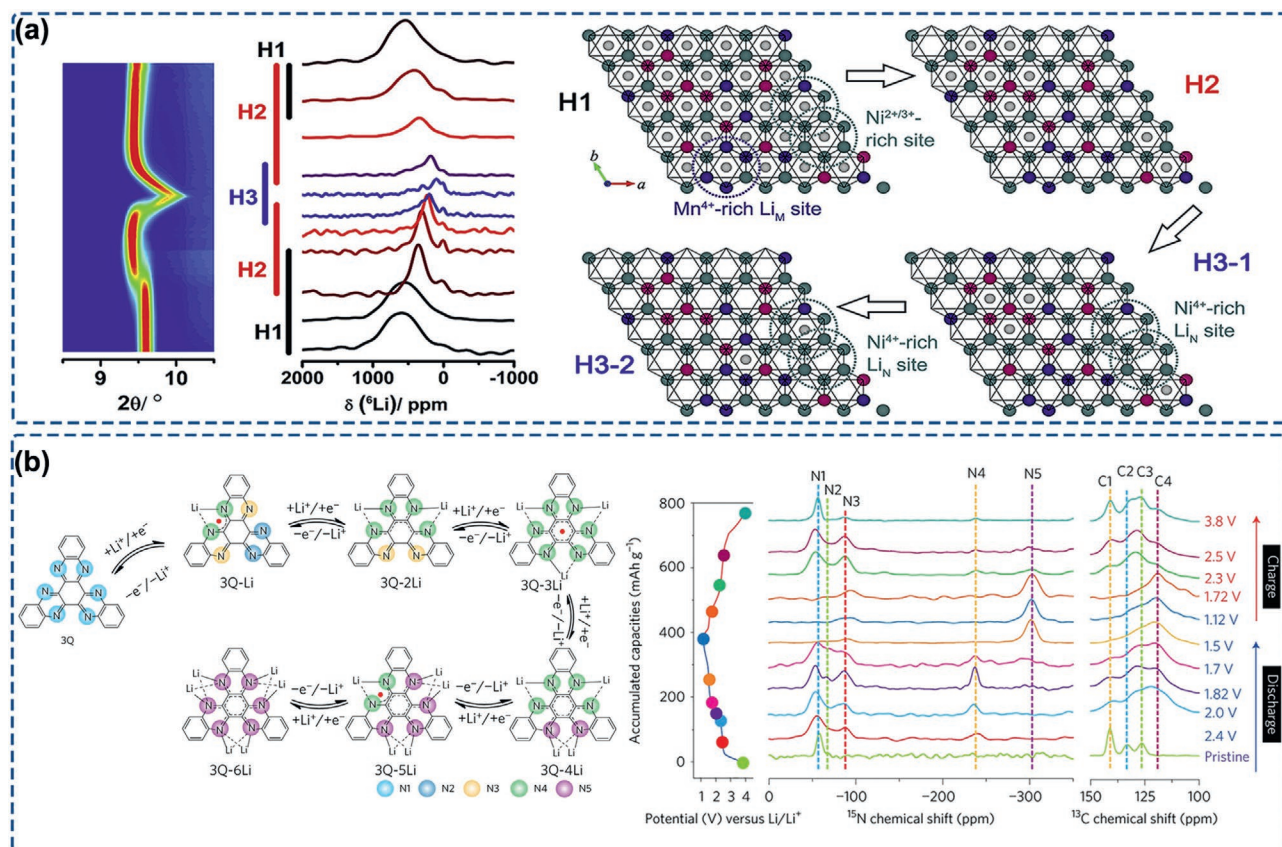


**Figure 3.** The local structural evolutions of electrode materials during cycling. a) In situ XRD (left),  $^6\text{Li}$  NMR spectra (middle) and schematic of the H1-H2-H3 phase transformation from the perspective of local environment along c axis of NCM622 (right). Reproduced with permission.<sup>[39a]</sup> Copyright 2019, Elsevier. b) The predicted lithiated structures and ex situ  $^{15}\text{N}$  and  $^{13}\text{C}$  NMR spectra of 3Q electrode during the discharging process. Reproduced with permission.<sup>[40]</sup> Copyright 2017, Nature Research.

the poly(2,5-dihydroxyl-1,4-benzoquinonyl sulfide) (PDBS) with the disappearance of C-Cl (115, 110 ppm) resonances and the appearance of C-S (105 ppm) during the sulfurization reaction.<sup>[41c]</sup> Since the decrease of shielding effect of the neighboring carbon, the extraction of an electron from C-S $^{\delta+}$ -C structure of PDBS leads to the positive shift of C-S resonance during charging. Besides, the chemical shift of the C=O and C-OH at 182 ppm does not change during entire cycling, indicating that the framework of PDBS is stable. The multi-electron reaction in the organic electrode is expected to greatly increase the energy density of the battery.<sup>[40,42b]</sup> Peng et al. revealed five different  $^{15}\text{N}$  resonances occurring at the multi-electron charge process of  $\pi$ -conjugated quinoxaline-based heteroaromatic molecules (3Q) material.<sup>[40]</sup> As shown in Figure 3b, the DFT calculation predicts that there are six stages in the lithium intercalation process, including bidentate with single lithium ion (3Q-Li), bis-bidentate (3Q-2Li), tri-bidentate (3Q-3Li), tetra-bidentate (3Q-4Li), penta-bidentate (3Q-5Li), and hexa-bidentate (3Q-6Li). Thus, five different  $^{15}\text{N}$  resonances are observed in the  $^{15}\text{N}$  MAS NMR at different lithiation degrees, namely, N1 (the signal assigned to pristine 3Q without binding to Li), N2 (the signal due to the non-bonded pyrazine N situated furthest away from Li), N3 (the signal due to the nonbonded pyrazine N nearest to a co-shared Li-bonded bipyridinetype site), N4 (the signal due to the co-shared one-Li-bonded pyrazine N), and N5

(the signal due to the co-shared two-Li-bonded pyrazine N). The above results can also be confirmed by  $^{13}\text{C}$  MAS NMR spectra in Figure 3b, with three  $^{13}\text{C}$  resonances at  $\approx 126$  (C1),  $\approx 133$  (C2), and  $\approx 140$  ppm (C3), and a new signal at  $\approx 120$  ppm (C4) appears at the end of discharging, suggesting increased lithium coordination and a loss of aromaticity in the  $\pi$ -conjugated lithiated 3Q during the discharge processes.

#### 2.2.4. Sodium Polyanions Materials

NIBs have received increasing attention in recent years. Because sodium salt has much higher natural abundance than lithium salt but possesses similar chemical and physical properties. NIBs are widely deemed as a cheaper alternative to LIBs. ssNMR has been also successfully applied in the cathode materials of NIBs, including both the polyanions and transition metal oxides materials. Polyanions materials are the outstanding electrode materials due to their high operating voltage, stable crystalline structure, and excellent thermal stability. In recent years, researchers have used ssNMR to study a variety of polyanionic materials, such as phosphates,<sup>[44]</sup> fluorophosphate,<sup>[45]</sup> sulfate,<sup>[46]</sup> etc. Li et al. employed  $^{23}\text{Na}$  MAS NMR in combined with DFT calculation to characterize the structural evolution and reaction mechanism of  $\text{Na}_2\text{FePO}_4\text{F}$  (space group: *Pbcn*) material during

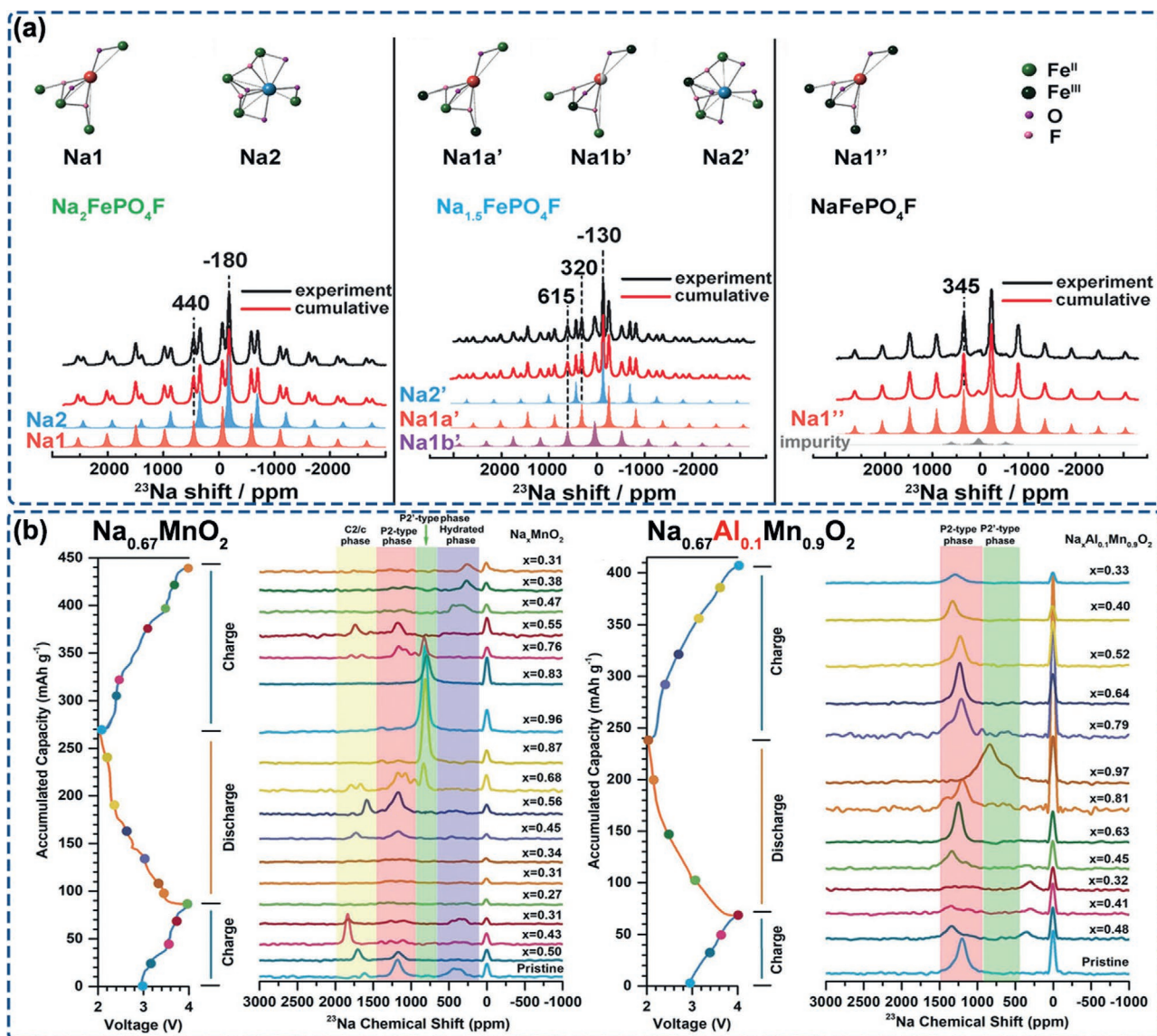


**Figure 4.** a) The  $^{23}\text{Na}$  local environment evolution of  $\text{Na}_x\text{FePO}_4\text{F}$  ( $x = 1, 1.5,$  and  $2$ ) materials. Reproduced with permission.<sup>[45e]</sup> Copyright 2018, Wiley-VCH. b) Ex situ  $^{23}\text{Na}$  NMR spectra during the initial charge-discharge cycles of  $\text{Na}_{0.67}\text{MnO}_2$  and  $\text{Na}_{0.67}\text{Al}_{0.1}\text{Mn}_{0.9}\text{O}_2$ . Reproduced with permission.<sup>[31b]</sup> Copyright 2019, Wiley-VCH.

the electrochemical reaction (Figure 4).<sup>[45e]</sup> The isotropic chemical shifts of different Na sites in the  $\text{Na}_{2-x}\text{FePO}_4\text{F}$  structure were identified through the local environment and line shifts as well as the profiles of spinning sidebands. Furthermore, the paramagnetic chemical shifts calculated by hybrid generalized DFT confirmed the accuracy of the above assignments. The ex situ  $^{23}\text{Na}$  NMR spectra (Figure 4a) show that, the  $\text{Na}^+$  ions at the Na1 site of the  $\text{Na}_2\text{FePO}_4\text{F}$  material are not electrochemically active, while the Na ions at the Na2 site are electrochemically active and reversible intercalation/extraction during charge and discharge processes. More importantly,  $\text{Na}_2\text{FePO}_4\text{F}$  electrode undergoes two two-phase reactions with an intermediate phase  $\text{Na}_{1.5}\text{FePO}_4\text{F}$  (space group:  $P2_1/c$ ) during cycling, which have clarified the debated electrochemical reaction mechanism of  $\text{Na}_2\text{FePO}_4\text{F}$  material.

## 2.2.5. Sodium Layered Oxides

Sodium layered oxides are considered as a cost-effective candidate for NIBs and have been most extensively studied.<sup>[47]</sup> Since the relative large size difference between  $\text{Na}^+$  ( $\approx 1.02$  Å) and TM ions (0.5–0.7 Å), the separation between Na and TM layers is easy to achieve without the ions-mixing phenomenon and almost all 3d TM ions can have the redox activity in layered  $\text{Na}_x\text{TMO}_2$  materials. However, the electrochemical performances of O3/P2/P2'- $\text{Na}_{0.67}\text{MnO}_2$  are still far from expectations due to the strong Jahn–Teller effect associated with  $\text{Mn}^{3+}/\text{Mn}^{4+}$  redox couple. It is expected that  $\text{Al}^{3+}$ -doping reduces the  $\text{Mn}^{3+}$  Jahn–Teller centers and expands the interspacing of  $\text{Na}^+$  layers thus accelerating the movement of  $\text{Na}^+$ . Liu et al. successfully developed the high-rate P2- $\text{Na}_{0.67}\text{Al}_x\text{Mn}_{1-x}\text{O}_2$  materials by a sol-gel



and post-quenching approach.<sup>[31b]</sup> As shown in Figure 4b, the NMR signals located at around 250–600, 650–900, 900–1400, and 1400–1850 ppm correspond to the hydrated, P2' (*Cmcm*), P2 (*P6<sub>3</sub>/mmc*), and C2/*c* phases, respectively. Without any electrode modification, the Na<sub>0.67</sub>MnO<sub>2</sub> electrode is dominated by severe biphasic transitions during the Na<sup>+</sup> (de)intercalation, involving the evolution of C2/*c* structures and P2-P2' transformation during Na<sup>+</sup> (de)intercalation. In contrast to Na<sub>0.67</sub>MnO<sub>2</sub>, the C2/*c* phase signal is absent in the <sup>23</sup>Na NMR spectra and the P2' phase can only be observed as *x* = 0.97 for Al doping Na<sub>0.67</sub>Al<sub>*x*</sub>Mn<sub>1-*x*</sub>O<sub>2</sub> electrode. Except for Al doping, other aliovalent doping elements exhibit similar effects of suppressing or delaying the appearance of P2' phase, such as Li<sup>+</sup>,<sup>[20,48]</sup> Zn<sup>2+</sup>,<sup>[49]</sup> Mg<sup>2+</sup>,<sup>[50]</sup> etc. Liu et al. have further explored the effects of various doping elements and different cooling rates on structural and electrochemical properties of Na<sub>*x*</sub>MnO<sub>2</sub> materials by combining XRD and ssNMR measurements.<sup>[51]</sup> Their results show that the undoped material with the rapid cooling treatment exhibited the largest capacity but had poor cycle performance, while slow cooling treatment and low-valent ions doping would effectively suppress the P2' phase, to extend cycling stability, but compromised the capacity. Thus, a rational element substitution should be implemented to mitigate Jahn–Teller effect and balance between the specific capacity and cycling stability to achieve superior electrochemical performance.

#### 2.2.6. Carbon Materials

Owing to the low price and outstanding structural adjustability, carbon materials have become one of the most popular anode materials for researchers and battery manufacturers. ssNMR was successfully applied in carbon materials more than 40 years ago. Conard et al. first reported the <sup>7</sup>Li NMR study of LiC<sub>6</sub> formed by lithium embedded in graphite and found that the chemical shift of LiC<sub>6</sub> compound is around 45 ppm, and the other signal at 0 ppm correspond to the Li<sup>+</sup> adsorbed on the graphite surface or in the SEI layer.<sup>[52]</sup> The <sup>7</sup>Li chemical shift of lithium intercalation compounds is highly relative with the microstructure of carbon materials. Mori et al. pointed out that there are two types of signals in disordered carbon materials.<sup>[53]</sup> One type has a wider peak width labeled as S site, and the other narrower peak is called C site. The Li<sup>+</sup> ions of C site are located in the parallel layers, while the Li<sup>+</sup> ions of S site are located on the surface or in the microcavity. Furthermore, the Li<sup>+</sup> ions of C site are easier to extract than that of S site. Fujimoto et al. found that lithium deposition did not occur in the hard carbon material under over-discharge state of 110%, while the graphite negative electrode showed the deposition of metallic lithium only under over-discharge state of 105%.<sup>[54]</sup> Therefore, using hard carbon as an anode electrode material is safer than graphite for LIBs. Although graphite almost cannot store Na<sup>+</sup> ions electrochemically, the intercalation of Na<sup>+</sup> can be also achieved by adding appropriate solvent molecules. Recently, Leifer et al. studied the influence of diglyme solvent molecules on graphite anode.<sup>[55]</sup> Their <sup>7</sup>Li, <sup>13</sup>C, and <sup>23</sup>Na NMR spectra prove that Li<sup>+</sup> and Na<sup>+</sup> would combine with the diglyme molecules to co-embed into the graphite layers and the coupling effect of solvent molecules with Li<sup>+</sup> is stronger than that of Na<sup>+</sup>,

thus the mobility of Li<sup>+</sup> is lower, which explains the reason why NIBs show the better electrochemical performance in diglyme solvent. Hard carbon materials demonstrate good reversible capacity and are among the cheapest proposed anode materials for NIBs. Stratford et al. successfully observed metallic sodium environments in both in situ and ex situ <sup>23</sup>Na NMR spectra, in which a new signal grows in intensity and proceeds gradually to higher shift at voltage lower than 180 mV, confirming the formation of metallic species within the pores of hard carbon materials at low voltage.<sup>[56]</sup>

#### 2.2.7. Li-Alloy and Their Composite Materials

Compared with intercalation reaction, alloying reaction can exhibit a higher Li<sup>+</sup> uptake due to the fact that alloying anode materials usually show the multiple-electron valence transition during cycling. Silicon (Si) materials possess larger theoretical specific capacity (4200 mAh g<sup>-1</sup>), but their volume will expand to about 300% during the charge and discharge process, resulting in the contact failure between particles and current collector, low Columbic efficiencies and rapid capacity decline. Grey's group used in situ and ex situ <sup>7</sup>Li NMR techniques, for the first time, to investigate the structural changes of silicon materials under the first discharge process.<sup>[57]</sup> The results showed that the Si anode would form Si–Si clusters and disperse Si atoms at the beginning of Li<sup>+</sup> intercalating. With the further insertion of Li<sup>+</sup>, the Si–Si clusters are crushed into dispersed Si atoms totally and then the crystal phase (Li<sub>15</sub>Si<sub>4</sub>) is formed (Figure 5a). It is worth noting that the formation of these amorphous Li<sub>*x*</sub>Si phases cannot be observed in the XRD patterns, but it shows a clear chemical shift difference from –15 to 20 ppm in <sup>7</sup>Li NMR spectra. Similarly, Tang et al. carried out in situ <sup>7</sup>Li NMR experiments to unravel the amorphous-to-crystalline transition mechanism in the germanide (Ge) material. The <sup>7</sup>Li resonances at 24, 13, 10, and –24 ppm are assigned to Li<sub>2.26</sub>Ge (amorphous), Li<sub>3.5</sub>Ge (amorphous), Li<sub>15</sub>Ge<sub>4</sub> (crystalline), and Li<sub>15+*θ*</sub>Ge<sub>4</sub> (overlithiated), respectively. Therefore, the lithiation process of Ge anode could be described as c-Ge → a-Li<sub>2.26</sub>Ge → a-Li<sub>3.5</sub>Ge → c-Li<sub>15</sub>Ge<sub>4</sub> + a-Li<sub>3.5</sub>Ge → c-Li<sub>15+*θ*</sub>Ge<sub>4</sub> + a-Li<sub>3.5</sub>Ge.<sup>[58]</sup>

Silicon monoxide (SiO) has become the next promising Si-based anode because SiO<sub>2</sub> as the buffer layer surrounding Si domains could reduce the volume change. Recently, Grey's group further compared the structure difference of pure-Si and SiO anodes during cycling (Figure 5b).<sup>[59]</sup> It is worth noting that the crystalline Li<sub>15</sub>Si<sub>4</sub> is formed through a two-phase reaction for pure-Si electrode with the significant voltage hysteresis and phase change. In contrast, the characteristic metallic Li<sub>*x*</sub>Si phase is gradually formed around 20 ppm on the SiO electrode, therefore the more continuous local structural evolution is considered as the main reason for the good cyclability of SiO electrode.

Phosphorus also belongs to the category of alloy anode, which has the theoretical specific capacity (2596 mAh g<sup>-1</sup>, referring to phosphorus anode and the final formation of Li<sub>3</sub>P) approximately seven times higher than that of graphite anodes (372 mAh g<sup>-1</sup>). However, phosphorus anode still suffer from poor cycle performance. In order to get insights into its decay mechanism, Pend et al. performed <sup>7</sup>Li and <sup>31</sup>P



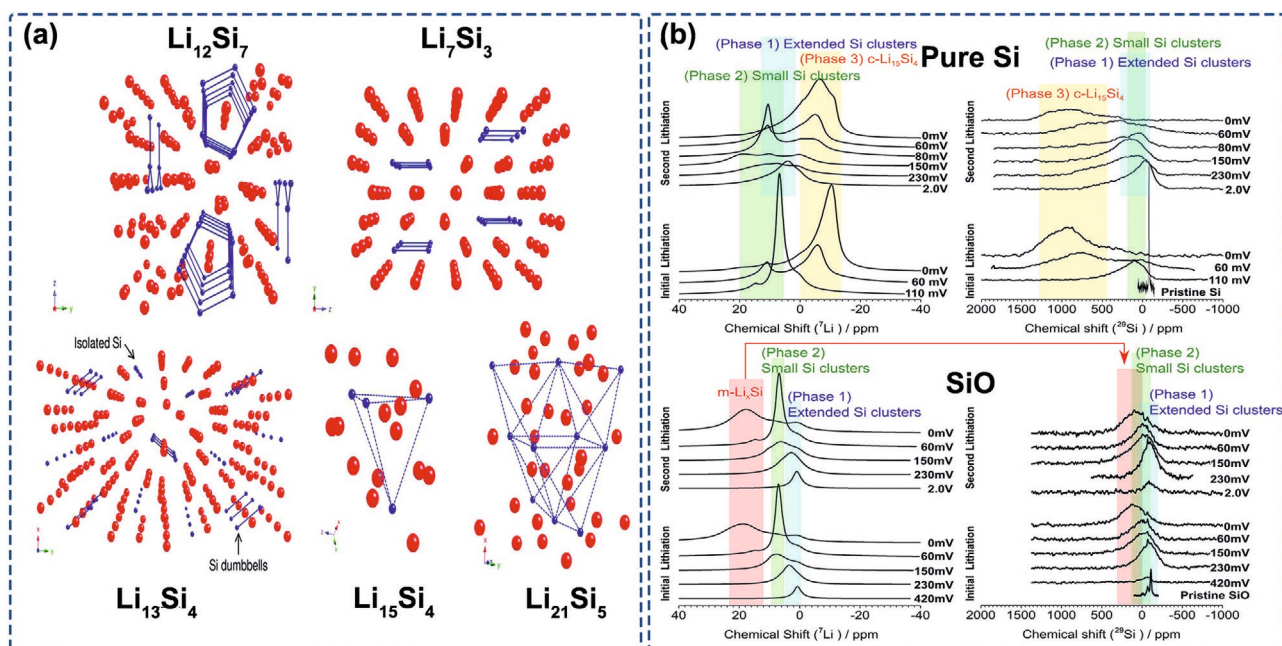


**Figure 5.** a) Schematic diagrams of different phase structure of pure-Si anode after lithium insertion. Reproduced with permission.<sup>[57]</sup> Copyright 2009, American Chemical Society. b) Ex situ  $^7\text{Li}$  and  $^{29}\text{Si}$  MAS NMR spectra of pure-Si and SiO during 1st and 2nd lithiation processes. Reproduced with permission.<sup>[59]</sup> Copyright 2019, American Chemical Society.

MAS NMR together with XRD to monitor the local and long-range structural evolution during cycling.<sup>[31]</sup> According to the evolution of  $^{31}\text{P}$  chemical shifts, they speculated the existence of the amorphous  $\text{Li}_3\text{P}$  ( $\alpha\text{-Li}_3\text{P}$ , -289 ppm) and overlithiated  $\text{Li}_{3+x}\text{P}$  (3.4 and -273.7 ppm) phases. And the alloying process ( $\text{rP} \rightarrow \text{LiP}_7 + \text{LiP}_5 + \text{Li}_3\text{P}_7 + \text{LiP} \rightarrow \alpha\text{-Li}_3\text{P} \rightarrow \text{c-Li}_3\text{P} \rightarrow \text{Li}_{3+x}\text{P}$ ) of phosphorus anode is different from the dealloying process ( $\text{Li}_{3+x}\text{P} \rightarrow \text{cLi}_3\text{P} \rightarrow \text{LiP}_7 + \text{LiP}_5 + \text{Li}_3\text{P}_7 + \text{LiP} \rightarrow \text{rP}$ ). Particularly, the low Columbic efficiency of phosphorus anode is assigned to the remaining of partial  $\text{LiP}_7$  phase and  $\text{Li}_3\text{PO}_4$  on the surface at the end of charge.

### 2.3. First-Principles Calculations of Paramagnetic Materials

Different from the quantitative information in the NMR spectrum that can be obtained by integrating the peak area and calibrating with  $T_2$  value,<sup>[28a]</sup> the assignment of chemical shift often requires the support of NMR calculations, especially for the metastable substance or mesophase appearing during electrochemical cycling that are unstable and difficult to synthesize. The local magnetic field strength of probed nucleus is measured through nuclear magnetic resonance and Zeeman energy level splitting. As the perturbation of external field, the internal field of materials can be contributed to multiple effects depending on the electronic structure of systems.<sup>[60]</sup> Particularly, the cathode material usually relies on TM ions for charge compensation, which contains localized unpaired electrons that lead to broad range of chemical shift and difficulty in signal deconvolution. Therefore, highly efficient density functional theory (DFT) methodology is urgently required for the rational assignment of peaks in those paramagnetic systems.<sup>[61]</sup> Due to

the relatively simple crystal structure of the phosphate materials and its ions hopping is in the slow chemical exchange regime, phosphate material is a good model system for verifying the accuracy of the calculation methods. In this section, the development of paramagnetic shift (PNMR) calculations for a series of phosphate materials is presented, while the detailed theory can be found elsewhere.<sup>[62]</sup>

The spin density transfers from unpaired electrons to observed nucleus, resulting in PNMR separation. Kim et al.<sup>[63]</sup> first calculated the so-called Fermi-contact (FC) shift in cathode materials by using DFT methodology. Combining all electron linear combinations of atomic orbitals (LCAO) method and B3LYP based hybrid functional, the computational shifts shows good qualitative agreement with experimental  $^7\text{Li}$  shift of several Fe (III) phosphates based LIBs cathode materials (Figure 6a). However, the calculated FC shift highly depends on Hatree-Fock (HF) exchange contents in hybrid functional, and the experimental or DFT optimized structures could also lead to remarkable shift difference. Therefore, it is necessary to check the computational shift with different Hatree-Fock (HF) exchange contents and geometry schemes. Actually, the unpaired electrons of Fe (III) 3d-orbital are high spin state and half filled, leading to symmetric 3d-orbital occupation ( $d^5$ ) that has small spin-orbital coupling and zero field splitting (ZFS) effect, thus the FC shift is a reasonable assumption at this circumstance. After that, Boucher et al.<sup>[64]</sup> calculated the  $^7\text{Li}$  FC shift of a series of  $\text{LiTMPO}_4$  (TM = Mn, Fe, Co, Ni) materials. Comparing with experimental shifts, on-site hybrid functional applied on TM ions and oxygen shows the best agreement for the cases of TM = Mn, Fe, Ni, while  $^7\text{Li}$  shift is overestimated significantly for TM = Co, leading to a  $^7\text{Li}$  shift sequence:  $\delta_{\text{LiMnPO}_4} > \delta_{\text{LiFePO}_4} > \delta_{\text{LiCoPO}_4} > \delta_{\text{LiNiPO}_4}$  that is inconsistent with

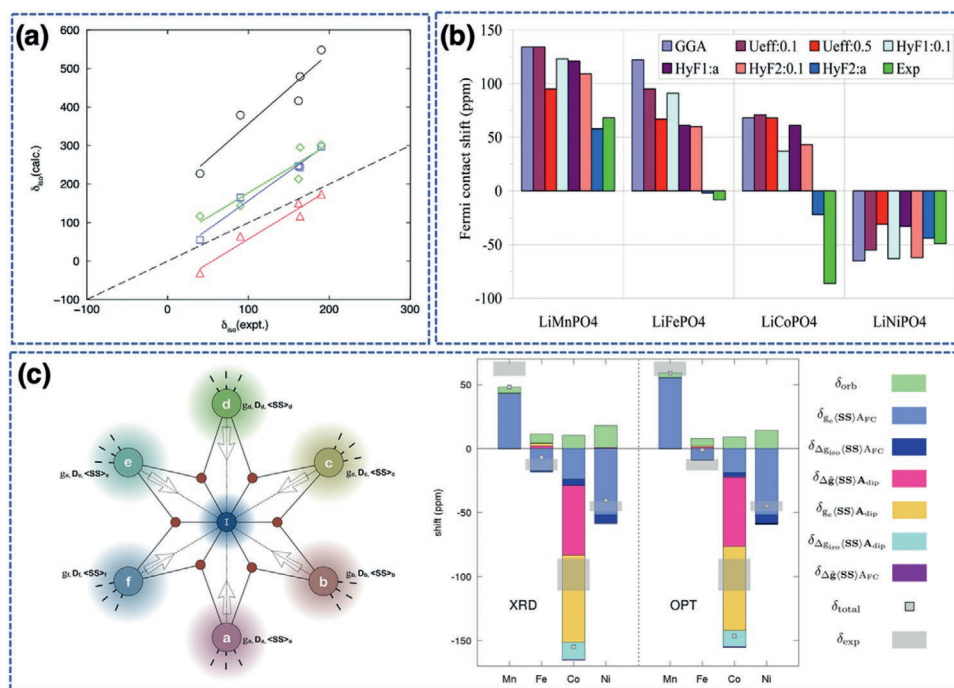


**Figure 6.** a) Correlations of the calculated  ${}^7\text{Li}$  FC shifts of Fe (III) phosphates for various exchange-correlation functional and geometry scheme with the experimental shifts. Reproduced with permission.<sup>[63]</sup> Copyright 2010, American Chemical Society. b) Comparison of experimental  ${}^7\text{Li}$  shifts of olivine  $\text{LiTMPO}_4$  (TM = Mn, Fe, Co, and Ni) with computational  ${}^7\text{Li}$  FC shifts. Reproduced with permission.<sup>[64]</sup> Copyright 2012, American Chemical Society. c) Diagram of coupling between g-tensor and D-tensor. The computational components and experimental  ${}^7\text{Li}$  PNMR shifts of olivine  $\text{LiTMPO}_4$ . Reproduced with permission.<sup>[61c]</sup> Copyright 2019, American Chemical Society.

the experimental  ${}^7\text{Li}$  shift results:  $\delta_{\text{LiMnPO}_4} > \delta_{\text{LiFePO}_4} > \delta_{\text{LiNiPO}_4} > \delta_{\text{LiCoPO}_4}$  (Figure 6b). The existing qualitative error implies that  ${}^7\text{Li}$  FC shift may not dominate the PNMR shift in  $\text{LiTMPO}_4$ . The reason is that  $d^5-d^8$  occupations in octahedral field have different symmetries and the lower symmetric electrons occupation has larger spin-orbital coupling and ZFS effect, resulting in non-negligible pseudocontact (PC) shift via coupling between hyperfine tensor, g-tensor and D-tensor (Figure 6c). Taking  $\text{LiTMPO}_4$  (TM = Mn, Fe, Co, Ni) as model system, Mondal et al. has recently developed a quantum chemical methodology including spin-orbital coupling and ZFS effects. It turns out that  ${}^7\text{Li}$  shift of  $\text{LiCoPO}_4$  is dominated by the negative PC shift, which is neglected in the previous work.<sup>[60]</sup> Thus the qualitative correction results are obtained (Figure 6c). However, its wider application is limited by the lack of periodic code and high computational resource demanding for g-tensor and D-tensor, and exchange coupling constant between paramagnetic centers is still included by experimental parameters, potentially leading to a double counting problem.<sup>[61c]</sup>

### 3. Solid Electrolyte Interfaces on the Electrode Materials

Practical LIBs and NIBs are complex electrochemical systems with many components, reactions and contacts between different material components yielding various interfaces, which can be divided into the solid–solid, solid–liquid interface and so on. Ions and electrons flow through these interfaces and fulfill

the charge/discharge processes in the rechargeable batteries. Therefore, the chemical and physical properties of these interfaces, including composition, structure, ionic/electronic conductivity etc., critically determine the cycling performance of the batteries.<sup>[65]</sup> For example, it is well-documented that SEI formed on the graphite can transport  $\text{Li}^+$  ions but block the electron passage, which suppresses electrolyte decomposition and greatly improves the lifespan of batteries. Therefore, the clarification of SEI species and structures can greatly improve the understanding of the (electro)chemical processes in the batteries, but it is also very challenging for many analytic techniques, mainly due to the following scientific issues: i) buried interface, ii) trace amounts of the species, iii) amorphous phase, iv) sensitivity to moisture and electrons, and v) dependence on cycle conditions. Thus, a comprehensive understanding of the roles of SEI in the electrochemical processes of the battery materials, including its composition, formation/degradation mechanism and  $\text{Li}^+/\text{Na}^+$  transport mechanism etc., is urgently required for battery researchers. In the past decade, ssNMR, with its demonstrated ability to nondestructively detect the local structure and ionic dynamics of specific nuclei, has become an excellent tool for analyzing compositions of SEI and tracking ionic motions.

#### 3.1. Identification of Interfacial Species

Identifying the chemical composition of the interfaces is a fundamental and critical step of disclosing its important roles in the LIBs and NIBs. Multinuclear NMR methods, such as  ${}^1\text{H}$ ,

$^7\text{Li}$ ,  $^{13}\text{C}$ ,  $^{19}\text{F}$ ,  $^{31}\text{P}$ , etc., can provide fruitful information about the composition of SEI on various electrode materials.

For example, Si is a promising anode material with a high theoretical specific capacity and low working potential, but Si anode is not primed for practical application due to the large volume change during electrochemical cycling, resulting in unstable SEI layers and thereafter a fast capacity decay. To solve this problem, constructing a stable SEI layer on a volume-constrained Si nanoparticle is a promising approach. Through heat treatment, Zheng et al. artificially firstly constructed an amorphous  $\text{SiO}_x$  SEI layer with well-defined thickness on the native Si nanoparticles.<sup>[66]</sup>  $^{29}\text{Si}$  MAS NMR complemented with TEM analysis demonstrated that the thickness of this  $\text{SiO}_x$  layer increases with temperature and duration of heat treatment, and the electrochemical tests indicated the optimized thickness of  $\text{SiO}_x$  is about 5 nm. In addition, the in situ formed SEI by the decomposition of electrolytes is a promising and flexible method. It is well-documented that FEC additives can greatly improve the cycle performance of Si anodes. Jin et al. employed DNP NMR to study the organic components of FEC-derived SEI on the Si anodes comprehensively.<sup>[34b]</sup> They disclosed the presence of cross-linked polymers with FEC additives, which believed is the key to stabilize the SEI layer (Figure 7a). In addition to organic components of SEI, Li et al. used a series of  $^{31}\text{P}$  and  $^{19}\text{F}$  MAS NMR spectra to follow the cycling process of the Si anode and concluded that the addition of FEC can suppress the hydrolysis of  $\text{LiPF}_6$  and contribute to the formation of  $\text{LiF}$ , which is beneficial for stabilizing the Si/electrolyte interface.<sup>[67]</sup>

Beyond Si anode, Li metal anode can offer the highest theoretical specific capacity and the lowest redox potential.

The fragile and high-reactive interface of Li metal/electrolyte obstructs a clear understanding of its chemical composition. Zheng et al. used ex situ MAS NMR to explore the synergic effects of  $\text{LiPO}_2\text{F}_2$  and vinylene carbonate (VC) additives on the Li metal anode.<sup>[68]</sup> The quantitative  $^{31}\text{P}$  and  $^{19}\text{F}$  MAS NMR demonstrate the increase in the amount of P-O-F species when using dual additives, implying that the addition of VC is conducive to the decomposition of  $\text{LiPO}_2\text{F}_2$  and contributes to the improved cycle performance (Figure 7b). Hu et al. employed ex situ  $^6\text{Li}$  NMR to investigate the SEI components on the Li metal anode in the LiFSI-DME electrolyte systems.<sup>[69]</sup> The dominance of  $\text{LiF}$  in SEI was revealed by quantitative NMR in the concentrated 4M LiFSI/DME electrolyte while  $\text{LiF}$  is absent in the diluted 1 M LiFSI/DME systems. Similarly, MAS NMR has been widely used in investigating SEI species in different electrolyte systems, as summarized in recent reviews.<sup>[9a,69,70]</sup> Nevertheless, the trace amount of SEI is challenging for the conventional NMR experiments, which would take hours or even days to meet a satisfactory signal-to-noise ratio. In this regard, DNP is a promising technique capable of enhancing NMR signals by several orders of magnitude, depending on the observed nucleus.<sup>[26c]</sup> For example, the NMR signals of  $^1\text{H}$  and  $^{13}\text{C}$  can be amplified by up to 660 $\times$  and 2600 $\times$ , respectively. Leskes et al. first explore the feasibility of DNP technique in characterizing the SEI formed on reduced graphene oxide (RGO).<sup>[71]</sup> Using external organic radicals(dinitroxide radical) as the source of polarization, known as “exogenous DNP”, the  $^{13}\text{C}$  NMR signal of outermost SEI can be amplified under the microwave irradiation and greatly shorten the experimental time. Recently, Grey’s group applied MAS-DNP technique

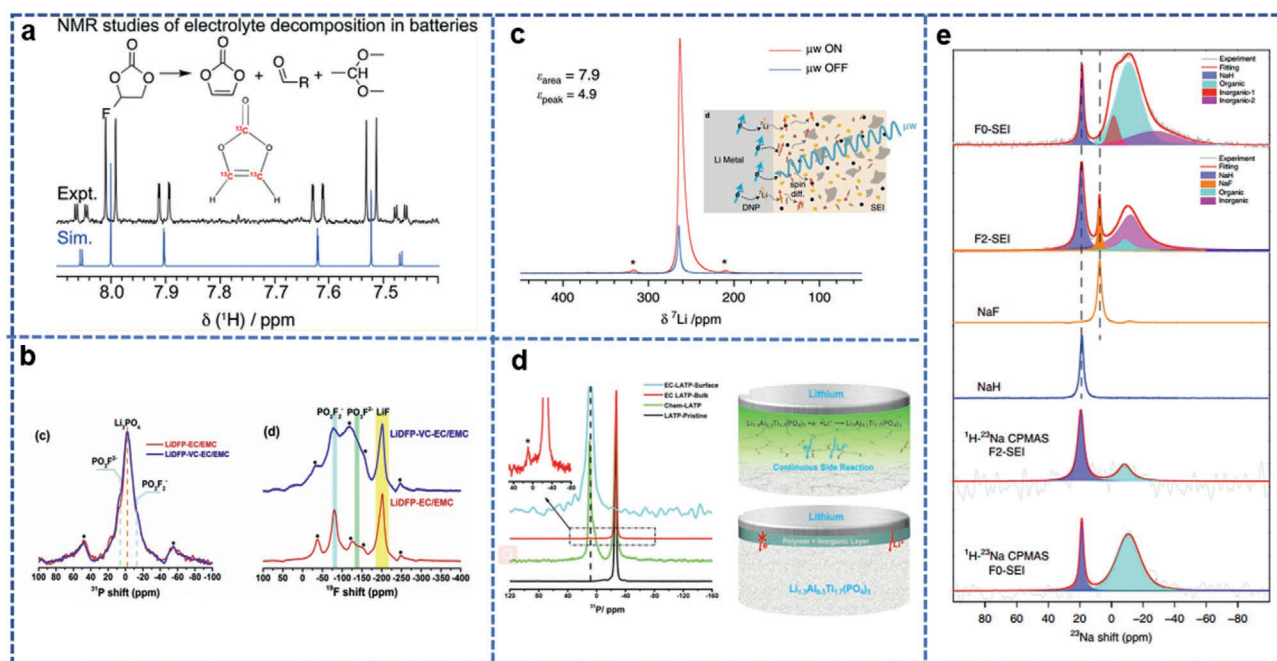


**Figure 7.** ssNMR studies on the composition of SEI layer. a)  $^{13}\text{C}$  NMR spectra of SEI species on the cycled Si anodes. Reproduced with permission.<sup>[34b]</sup> Copyright 2017, American Chemical Society. b)  $^{31}\text{P}$  and  $^{19}\text{F}$  MAS NMR spectra of SEI species derived from dual additives. Reproduced with permission.<sup>[68]</sup> Copyright 2020, Elsevier. c)  $^7\text{Li}$  MAS NMR spectra of Li metal with and without microwave irradiation. Reproduced under the terms of a Creative Commons Attribution 4.0 International License.<sup>[34a]</sup> Copyright 2020, The Authors, published by Springer Nature. d)  $^{31}\text{P}$  MAS spectra of LATP and reacted LATP samples. Reproduced with permission.<sup>[72]</sup> Copyright 2020, American Chemical Society. e)  $^{23}\text{Na}$  MAS and  $^1\text{H}$ - $^{23}\text{Na}$  cross-polarization MAS spectra of SEI formed on the sodium metal anode. Reproduced with permission.<sup>[32]</sup> Copyright 2020, Nature Research.



to investigate the Li metal/electrolyte interface.<sup>[34a]</sup> Different from the exogenous DNP, the internal electrons of Li metal can serve as the source of polarization named as “Endogenous DNP”. As shown in Figure 7c, the signal of Li metal is amplified by DNP to 7.9 (based on the peak area) compared to the conventional NMR test. This work demonstrates that DNP is a feasible way to investigate trace amount species in lithium metal batteries (LMBs) and can be extended to study the buried interface in solid-state batteries (SSBs), which is more challenging due to the limited light/electron permeability of SSBs. As mentioned above, ssNMR proves that the sulfide SEs is prone to spontaneous decomposition reaction during the preparation process of the composite electrode.<sup>[14]</sup> In addition, the narrow electrochemical window of SSEs would lead to a serious reaction between SSEs and Li metal. <sup>6</sup>Li and <sup>31</sup>P MAS NMR further confirmed that LSPS is reduced into Li<sub>2</sub>S, Li<sub>3</sub>P and Li<sub>3+x</sub>P after cycling with Li metal, but a similar or even much shorter T<sub>1</sub> of these decomposition products as opposed to of pristine LSPS suggests that the increased interfacial resistance should be mainly attributed to the porous and loose surface morphology.<sup>[14]</sup> Zhu et al. employed <sup>7</sup>Li, <sup>31</sup>P and <sup>27</sup>Al MAS NMR spectra to investigate reaction-process between the Li<sub>1.3</sub>Al<sub>0.3</sub>Ti<sub>1.7</sub>(PO<sub>4</sub>)<sub>3</sub> (LATP) and Li metal anode.<sup>[72]</sup> A Li-rich LATP as an interfacial species is experimentally clarified after LATP cycled with Li metal (Figure 7d). The Li-rich LATP has improved electronic conductivity compared to LATP and cannot passivate the Li metal, leading to continuous side reactions at the interface and thus rapid cell failure.

The continuous unveiling of new species undoubtedly can deepen the understanding of interfacial reactions, especially for clarifying the controversial results of the existence of hydrides in the interface layer.<sup>[73]</sup> For instance, Hu et al. used multinuclear and multidimensional ssNMR to disclose the presence of LiH on the RuO<sub>2</sub> electrode, and found that the extra capacity of RuO<sub>2</sub> comes from the generation of LiOH and its conversion reaction to form Li<sub>2</sub>O and LiH.<sup>[74]</sup> Recently, as shown in Figure 7f, Xiang et al. used quantitatively <sup>23</sup>Na MAS NMR and <sup>1</sup>H-<sup>23</sup>Na cross polarization NMR techniques demonstrate that NaH exists as a major interfacial species on the surface of sodium metal anode.<sup>[32]</sup>

Compared to the SEI species, another interfacial species called “Dead Li metal” formed during stripping process is more substantive, which is considered as the major culprit of capacity loss of LMBs in a recent interesting research.<sup>[73a]</sup> <sup>7</sup>Li MAS NMR was recently employed to study the formation of dead Li metal, benefited from the large difference in NMR chemical shifts between dead Li metal (≈260 ppm) and Li-bearing SEI species (≈0 ppm).<sup>[75]</sup> Chen et al. found a dominant signal of dead Li metal in the interfacial species, collected from Cu foil in the Li||Cu cells after 20 cycles when using LiPF<sub>6</sub>/EC:DEC electrolytes.<sup>[76]</sup> In contrast, the signal of dead Li metal can be completely eliminated by using the concentrated 5 M LiFSI/EC:ETFECEC electrolyte.

### 3.2. Ionic Transport across the Interface

In addition to the interfacial species, the transport rate and path of ions across the interface need to be further studied in order to establish the correlations between the function

of interface and the performance of the LIBs and NIBs. The nuclei-specified ssNMR is sensitive to the ionic motion at atomic level, thus can be adopted to investigate the ionic transport at the interface. Yu et al. employed 2D-EXSY to investigate ionic transport between Li<sub>2</sub>S cathode and Li<sub>6</sub>PS<sub>5</sub>Br solid-state electrolyte.<sup>[28b]</sup> Different processing methods are investigated, indicating that nanosizing and ball-milling can improve the interfacial ionic transport while electrochemical cycling can obstruct it. Following this study, Cheng et al. conducted a quantitative study of the space charge layer effect on the interface between Li<sub>x</sub>V<sub>2</sub>O<sub>5</sub> cathode and LAGP solid electrolyte by adjusting the chemical potential of Li<sub>x</sub>V<sub>2</sub>O<sub>5</sub> (Figure 8a).<sup>[33]</sup> They also exquisitely used 2D-EXSY to monitor the characteristics of ion exchange at different chemical environments. Their results show that although the activation energy of Li<sup>+</sup> diffusion in the Li<sub>2</sub>V<sub>2</sub>O<sub>5</sub> bulk phase is lower than that of LiV<sub>2</sub>O<sub>5</sub>, its chemical potential is higher than that of LAGP, resulting in the formation of a space charge layer at the Li<sub>2</sub>V<sub>2</sub>O<sub>5</sub>-LAGP interface. The low intensity of off-diagonal exchange peak suggests that the exchange of Li<sup>+</sup> at this interface is hindered. However, LiV<sub>2</sub>O<sub>5</sub> has the same chemical potential as LAGP, thus there is no space charge layer at the LiV<sub>2</sub>O<sub>5</sub>-LAGP interface. Consequently, 2D-EXSY shows a higher intensity of off-diagonal exchange peak.

Furthermore, isotope labeling combined with ssNMR is another common method used to characterize ionic transport. Jerschow et al. immerse the <sup>6</sup>Li metal in natural abundance electrolyte to observe the spontaneous <sup>6</sup>Li/<sup>7</sup>Li exchange.<sup>[77]</sup> After that, Gunnarsdottir et al. studied the additives effect on the ionic transport between non-aqueous electrolyte and Li metal (Figure 8b).<sup>[78]</sup> With FEC additives, the <sup>6</sup>Li/<sup>7</sup>Li exchange is twice fast compared to the standard electrolyte (LiPF<sub>6</sub>/EC:DMC). Isotope labeling combined with ssNMR method offers a quantitative understanding on the exchange rate at the interface. Nevertheless, the above study on the transport properties are all conducted without current flowing, that is, the spontaneous transport is focused. While in operating LIBs, Li ions transport across the interface take place under an external electric field. In this regard, the development of operando NMR technique to study the interfacial transportation is essential.

## 4. In Situ NMR Characterization of Electrochemical Processes

LIBs and NIBs are complicated devices because multiple electrochemical and chemical processes concurrently take place and correlate with each other. Untangling and understanding these coupled processes are key to explain how batteries fail and how to improve their performance. In situ NMR and MRI techniques are able to collect data when the batteries in operation, which exhibit many advantages over ex situ experiments where the cell cycling has to be stopped for extracting the electrode.<sup>[6a]</sup> In this section, the advantages and challenges of in situ NMR and MRI techniques are firstly discussed, then some examples are presented, the requirements and development of in situ cells are summarized in the end.

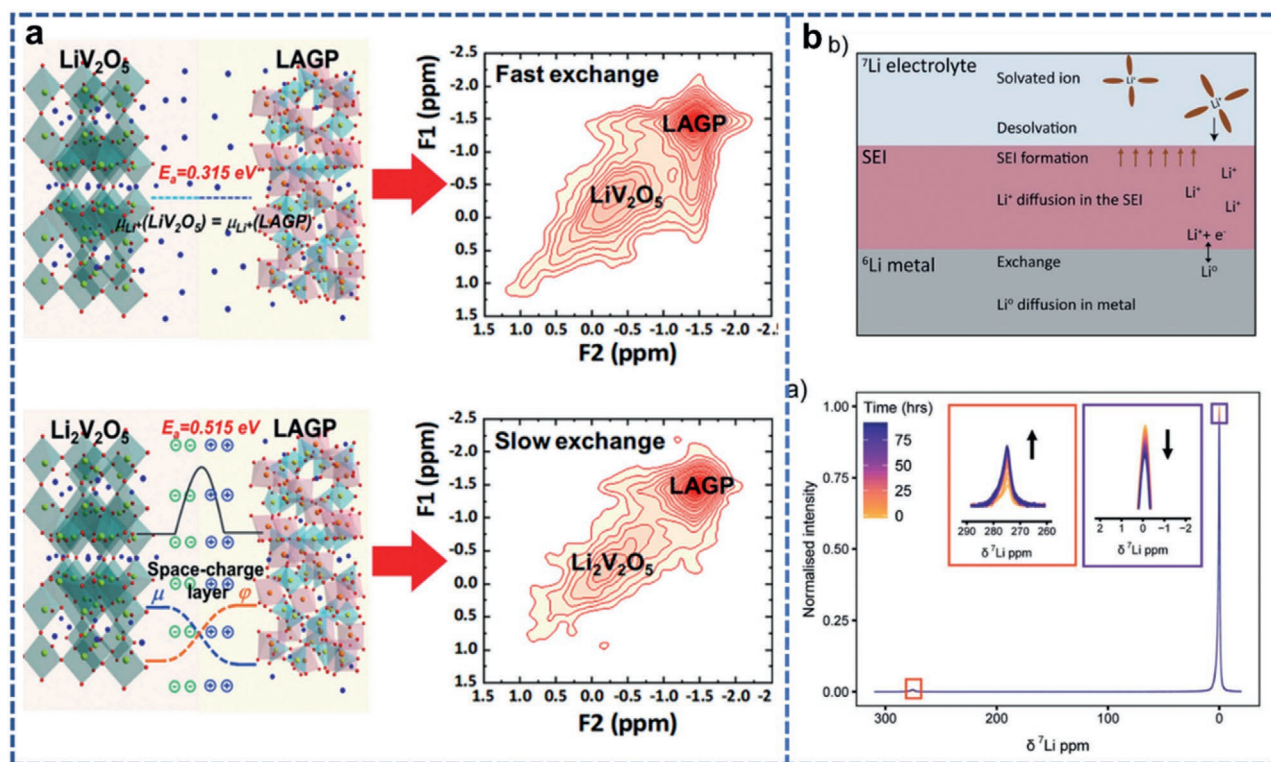


**Figure 8.** ssNMR study on the interfacial transport. a) The effects of space charge layer on the ionic transport at the cathode/electrolyte interface, revealed by 2D EXSY NMR. Reproduced with permission.<sup>[33]</sup> Copyright 2020, Elsevier. b) Isotope labelling combined ss NMR to track ionic transport at the Li metal/electrolyte interface. Reproduced under the terms of the Creative Commons CC-BY license.<sup>[78]</sup> Copyright 2020, Royal Society of Chemistry.

#### 4.1. Advantages and Challenges of In Situ NMR and MRI

In situ NMR and MRI belong to non-invasive techniques, which avoid the loss of information due to the damage of internal structure during the disassembly processes and ensure the acquisition of real information taking place inside the battery. Moreover, the real-time data collections can obtain abundant dynamic information and enable to capture metastable or intermediate phases because they can minimize the process of self-relaxation, which is beneficial to get a deep insight into electrochemical mechanism. Similar to ex situ NMR, in situ NMR experiments identify the chemical species and enable to analyze both in crystalline and amorphous materials. Furthermore, kinetic information about ions diffusion can also be obtained through operando spin-lattice and spin-spin relaxometry.<sup>[79]</sup> As a result, in situ NMR has been extensively utilized in studying the cathode (transition metal oxide,<sup>[28a]</sup> polyanion compound,<sup>[45c]</sup> sulfur<sup>[80]</sup>, etc.) and anode (carbon,<sup>[81]</sup> silicon,<sup>[57]</sup> Li metal,<sup>[82]</sup> Na metal,<sup>[83]</sup> etc.), gaining unambiguous structure/phases evolution under working conditions.

In situ MRI, with the introduction of magnetic field gradients on the basis of NMR, possesses spatial resolution and enables to intuitively visualize spatial distribution of NMR signals, thus providing more elaborate information in real time.<sup>[84]</sup> At present, the applications of in situ MRI mainly focus on the ions distribution in electrolytes (liquid electrolytes<sup>[85]</sup> and solid-state electrolytes<sup>[36b]</sup>), the evolution of electrode materials

(paramagnetic cathode,<sup>[86]</sup> Li metal,<sup>[87]</sup> and Na metal<sup>[32]</sup>), and the diagnosis of commercial cells.<sup>[88]</sup>

Although in situ NMR and MRI techniques are of considerable promising in understanding the complex mechanism involving in batteries, they still have several limitations and challenges that need to be overcome before starting in situ experiments. First, the dramatic difference between the ex situ and the in situ experiments is that the sample can be spun in ex situ experiments (maximum  $\approx 110$  kHz) while is motionless in in situ experiments. Fast spinning could partially or totally eliminate some of the internal NMR interactions, giving rise to high resolution spectra. While a static sample tends to induce a broad resonance signal, such that in situ experiments have much lower spectral resolution than ex situ experiments. Especially due to the existence of the interaction between the unpaired electron of paramagnetic TM ions and the target nucleus such as  $^6,7\text{Li}$  in the cathode materials, the observed signal is considerably broad, which hinders the insightful investigation of cathode materials by in situ NMR. In addition, the chemical shift and line width are influenced by the orientation of in situ cell, which can be explained by the theory of bulk magnetic susceptibility (BMS) effects.<sup>[89]</sup> For example, the signal of lithium metal changes from 242 to 272 ppm when the angle between lithium strip and external field  $B_0$  changes from  $90^\circ$  to  $0^\circ$ . For cells containing paramagnetic materials, this situation is even more complicated.<sup>[90]</sup> Second, since the chemical shifts of various components in batteries are different, such as the  $^6,7\text{Li}$  signal of lithium salt in electrolytes and

lithium-contained compound in SEI is at around 0 ppm, while the signal of lithium metal anode is around 242 ppm and the signal of cathode materials covers a large range of up to several thousand ppm. It is challenging to uniformly acquire all of the signals (cathode, anode, electrolytes) because the radio frequency cannot excite the whole range effectively.<sup>[6a]</sup> In addition, the spatial resolution of in situ MRI is still low, only several tens or hundreds of micrometers, which is unsatisfied for gaining spatial information about composite electrode structure in the batteries.<sup>[84]</sup>

#### 4.2. The Application of In Situ NMR and MRI Techniques

Since the application of in situ NMR and MRI techniques for cathode is still difficult due to the poor spectral/spatial resolution in static mode, thus the current researches mainly focus on anode materials, including carbon, silicon, lithium metal, sodium metal, *etc.* As far as we know,  $\text{Li}^+$  intercalation voltage in the graphite is close to 0 V (versus  $\text{Li}^0/\text{Li}^+$ ). Therefore, in some certain operating conditions, such as low temperature and high current density, some  $\text{Li}^+$  cannot intercalate into the lattice of graphite instead form lithium metal microstructures (LMs) on the graphite/electrolyte interface, known as “Li plating” process. The formation of LMs not only causes capacity loss of LIBs but also brings safety hazards. ssNMR has its own unique advantages in studying the LMs owing the large difference in  $^7\text{Li}$  NMR chemical shift of LMs (270 ppm) and  $\text{LiC}_x$  ( $\approx 40$  ppm). By observing the signal around 270 ppm, one can directly investigate the formation and evolution of LMs. For example, Arai et al. used in situ  $^7\text{Li}$  NMR to observe the overcharge state of graphite and hard carbon electrodes.<sup>[91]</sup> They confirmed the “relaxation effect” of the negative electrode after overcharging, that is, the signal of Li metal deposited on the surface of the negative electrode would decrease over time. This effect was clearly observed in the first few hours. This work demonstrates the importance of in situ techniques for studying the LMs. Recently, this group further used  $^7\text{Li}$  in situ NMR technique to compare the relationship between the trigger time of LMs and overpotential on the graphite and hard carbon anode respectively. They disclosed that the lithium metal clusters are formed earlier than LMs, and the pores in hard carbon can provide a shelter for metal clusters, thus greatly delay the formation of LMs as compared to graphite.<sup>[92]</sup>

In situ NMR was also utilized to investigate the lithiation behavior of silicon.<sup>[57]</sup> It is found that metastable  $\text{Li}_{15+x}\text{Si}_4$  phase is formed at deep discharge and will be gradually converted into  $\text{Li}_5\text{Si}_4$  phase together with the reduction of electrolyte. Such information of a metastable phase is missing in the conventional ex situ experiments. In contrast to the graphite and silicon anode, the plating and stripping process of Li metal are the working mechanism of Li metal anode, which brings more serious challenges in safety concerns in LMBs. In 2010, Grey et al. developed in situ  $^7\text{Li}$  NMR to study the LMs in  $\text{Li}|\text{LiCoO}_2$  and  $\text{Li}|\text{Li}$  cells.<sup>[82]</sup> They clarified the skin-depth effects and BMS effects in the study of Li metal, thus firstly achieved the separation and quantification of bulk Li metal and LMs. Following this study, many strategies for relieving LMs are evaluated by in situ  $^7\text{Li}$  NMR, such as additives,<sup>[93]</sup> stack pressure,<sup>[94]</sup>

and using SSEs.<sup>[95]</sup> Hu et al.<sup>[93]</sup> separately quantified the vertically and horizontally deposited Li by in situ  $^7\text{Li}$  NMR and observed that more vertically porous nanofiber/nanorod Li formed after adding  $\text{Cs}^+$  additive. In situ  $^{133}\text{Cs}$  NMR further proved that  $\text{Cs}^+$  could migrate from electrolyte to electrode to form positively charged electrostatic shield. Chang et al.<sup>[94]</sup> found that dendritic LMs were not easily formed under external pressure, which is consistent with the results from in situ  $^7\text{Li}$  NMR that the  $^7\text{Li}$  NMR signal of LMs is lower than 270 ppm (270 ppm generally corresponds to dendritic LMs). Recently, Xiang et al. combined in situ  $^7\text{Li}$  NMR with practical anode-free batteries ( $\text{Cu}|\text{LiFePO}_4$ ) to distinguish and quantify the inactive Li during the whole cycling process.<sup>[96]</sup> This quantitative technique had also been used to monitor the inactive Li on the carbon anode materials.<sup>[97]</sup> In addition, LMs are morphologically non-uniform lithium deposits, thus the spatial information of LMs is critical in revealing their formation mechanism. Jerschow et al. developed  $^7\text{Li}$  MRI techniques to offer a spatial insight of LMs during cycling.<sup>[87]</sup> Then, Chang et al. correlated the onset time of Li dendrites with the applied current density by employing  $^7\text{Li}$  chemical shift imaging method, which experimentally validates the Sand's model at high current density and finds a separate model at low current density.<sup>[36a]</sup> Following this study, the formation of Li dendrites inside the solid-state electrolytes is investigated by  $^7\text{Li}$  MRI technique, to monitor the evolution process of Li dendrites from the onset to throughout the whole electrolyte (Figure 9a).<sup>[95]</sup> In addition to directly imaging the LMs by using  $^7\text{Li}$  signal, Jerschow ingeniously developed 3D  $^1\text{H}$  MRI techniques to reversely visualize the growth of LMs, which greatly increases the sensitivity of MRI technique by using  $^1\text{H}$  rather than the low-sensitivity nuclei  $^7\text{Li}$ .<sup>[98]</sup> This technique can be easily extended to the other metallic anode and the feasibility has been demonstrated in the study of sodium metal microstructures (SMs).<sup>[99]</sup> Compared to LMs, SMs are much less reported and studied, though there are some discussions emphasizing the distinctions between Li metal and sodium metal.<sup>[100]</sup> Recently, Xiang et al. used in situ MRI to explore the spatial distribution of SMs during Na deposition/stripping cycling (Figure 9b).<sup>[32]</sup> And operando  $^{23}\text{Na}$  NMR results prove that the increasing SMs firstly give a linear rise in deposition overpotential until reaching a transition overpotential of  $\approx 0.15$  V, at which a violent decomposition of electrolyte is triggered, leading to the formation of mossy-type SMSs and rapid battery failure.

#### 4.3. Requirements and Developments of In Situ Cell

The first step for carrying out in situ NMR experiments is to assemble in situ cell whose electrochemical performance should be as close as possible to that of practical coin cell to reflect the actual electrochemical process. In consequence, having a suitable in situ cell is prerequisite for conducting in situ experiments. Several requirements should be emphasized when designing in situ cell. The material used to make batteries must be non-magnetic and chemical stable toward cathode, anode, and electrolytes. Therefore, the use of polyetheretherketone (PEEK) is highly recommended due to its robustness, chemical stability, and processibility. Metal components



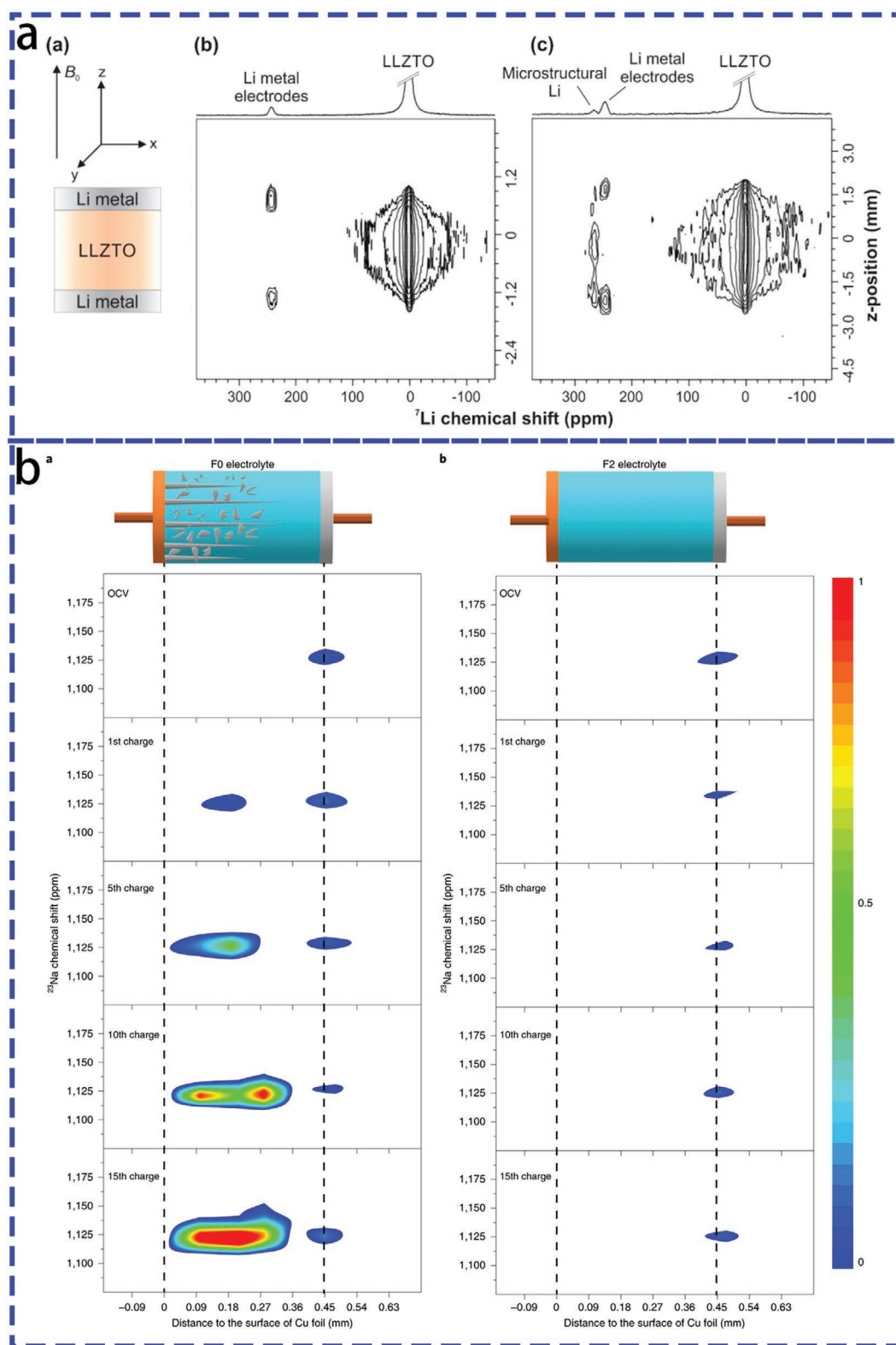


**Figure 9.** Investigation of Li/Na metal microstructures by in situ NMR. a) In situ  $^7\text{Li}$  MRI images for LLZO-based SSEs. Reproduced with permission.<sup>[95]</sup> Copyright 2019, American Chemical Society. b) In situ  $^{23}\text{Na}$  MRI for Cu||Na cells. Reproduced with permission.<sup>[32]</sup> Copyright 2020, Nature Research.

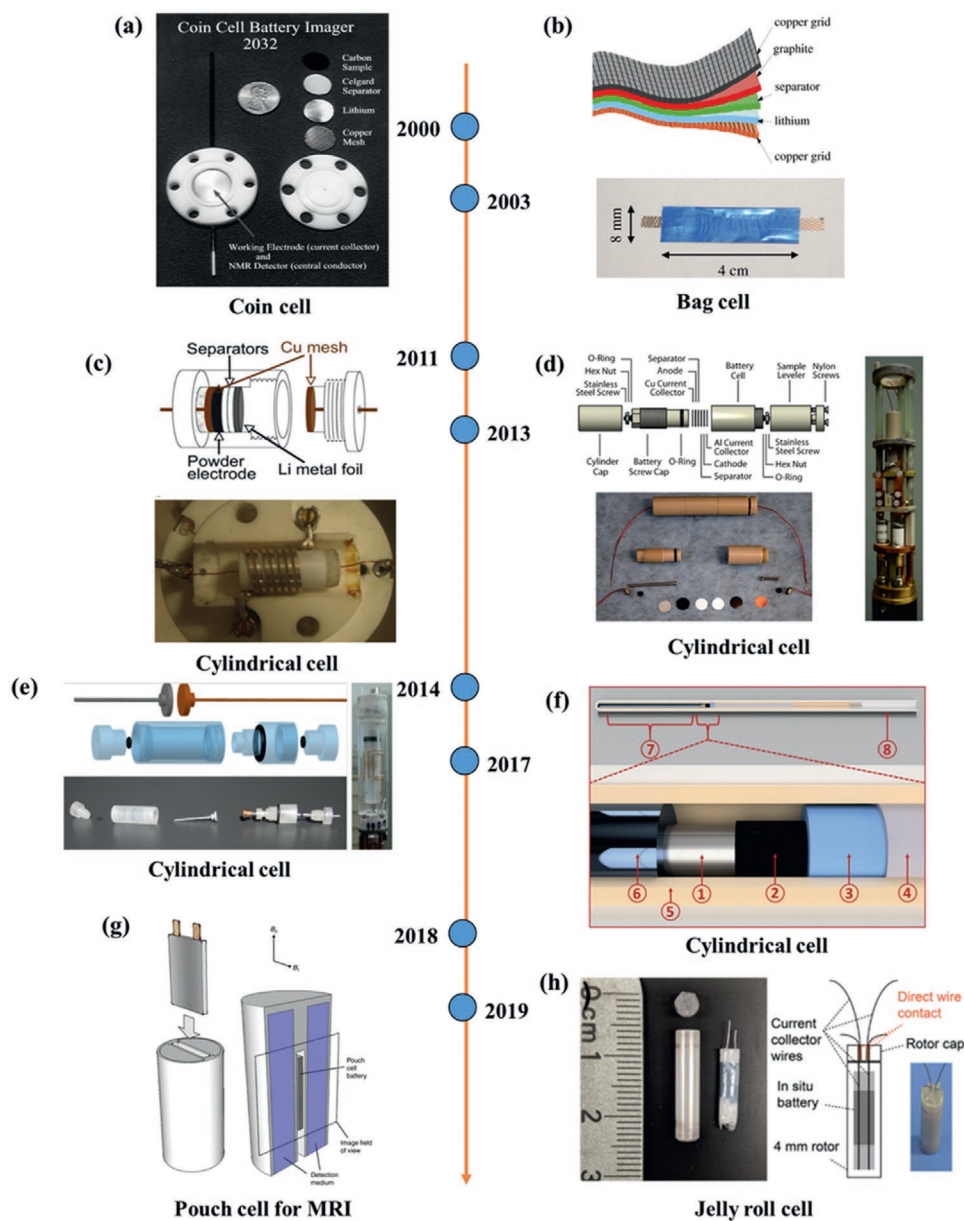


**Figure 10.** The development process of in situ cell. a) Coin cell in 2000. Reproduced with permission.<sup>[81]</sup> Copyright 2000, Elsevier. b) Bag cell in 2003. Reproduced with permission.<sup>[107]</sup> Copyright 2007, Elsevier. c–e) different designs of cylindrical cell.<sup>[102–104]</sup> c,d) Reproduced with permission.<sup>[102]</sup> Copyright 2011, Elsevier. e) Reproduced with permission.<sup>[104]</sup> Copyright 2014, American Chemical Society. f) Cylindrical cell for detecting liquid electrolyte. Reproduced with permission.<sup>[105]</sup> Copyright 2017, Royal Society of Chemistry. g) Pouch cell for MRI.<sup>[88]</sup> h) Jelly roll cell for in situ MAS NMR. g,h) Reproduced with permission.<sup>[35]</sup> Copyright 2019, American Chemical Society.

should be avoided as much as possible to allow the penetration of radio frequency (RF) pulses due to the so-called “skin effect”.<sup>[82]</sup> Thus, it is better to use metal mesh as current collectors. The battery should be impermeable against the air since trace of moisture will dramatically degrade the electrochemical performance of in situ cell. Moreover, the in situ cell should be able to maintain tight contact for a long time, which is crucial for realizing excellent electrochemical performance.

Several kinds of in situ cell have been reported in the literature and their configuration and development time are summarized in **Figure 10**. The first in situ NMR experiments

was implemented by Gerald et al.<sup>[81]</sup> in 2000 whose in situ cell setup is shown in Figure 10a. They designed standard 2032-size coin cell, in which metal shell is replaced with Teflon. The copper plate on one Teflon housing is served as both current collector and NMR detector. During NMR acquisition, the membrane separator and lithium counter electrode are extracted to minimize the signal of electrolytes, hence the cell was not in the working state when NMR acquisition was finished. Besides, the signal-to-noise ratio of spectra is too low to facilitate their further development. After that, Letellier et al.<sup>[101]</sup> adopted Bellocore-type plastic bag cell (Figure 10b)

and placed it in the conventional static NMR probe head with a 10 mm diameter coil. The application of conventional probe head could improve signal-to-noise ratio and simplify the setting up procedure of in situ NMR experiments. However, the assemble of bag cell is a cumbersome process, which involves making laminates of various cell components (cathode, anode, and separator), laminating the three components together, and sealing it into an air-tight plastic bag with current collectors. In addition, it is difficult to ensure good contact and airtightness of the cell. At the same time, electrolytes leakage is easy to happen, thus its electrochemical performance and reproducibility is poor. Then Letellier and coworkers further designed a new type of in situ cell, that is, cylindrical cell<sup>[102]</sup> as shown in Figure 10c. This new cylindrical cell has a cylindrical housing that is made of polypropylene, which only opens one side that is sealed with a screw type cap. Then current collectors are connected to the cap and the bottom through punched holes. Such a design effectively overcome the aforementioned problems in bag-type cell and the assembly of the battery becomes easier by placing cathode, separator, and anode successively into the cell and sealing it with screw type cap. The chances of electrolyte leakage are also decreased due to the reduced area required to seal. Based on the above advantages, its cyclability has been considerably improved. Subsequent development of in situ cells mainly focused on cylindrical cells, but with different design. In 2013, Tang et al.<sup>[103]</sup> reported a novel cylindrical cell made from PEEK (Figure 10d) for in situ stray-field-imaging (STRAFI), which can in situ monitor Li<sup>+</sup> movement. Salager et al.<sup>[104]</sup> devised a new cylindrical cell as shown in Figure 10e. New cell setup is vertically placed in probe head equipped with a saddle coil, which can receive the maximum penetration of RF. Moreover, 1D image along z axis can be carried out with this new design. As shown in Figure 10f, Wiermers–Meyer et al.<sup>[105]</sup> built a cylindrical cell inside a conventional NMR tube, which can be used to monitor liquid electrolytes. Kayser et al. further optimized the cylindrical in situ cell and significantly increased its cyclability to hundreds of cycles.<sup>[106]</sup> In 2018, in situ MRI with an inside-out mode was developed to assess different SOC and diagnose the flaws of commercial pouch cells (Figure 10g).<sup>[88]</sup> Since the RF cannot totally penetrate the conductor in commercial pouch cells, so they made it by detecting the induced or permanent magnetic field from the cell and then inferring what was going on inside the cell.

The mentioned in situ cells are in static mode during NMR acquisition normally leads to broad resonances and reduce the spectral resolution. Alternately, spinning the in situ cells under magic angle (54.7°) can effectively solve above problem. However, it is difficult to accomplish as the metallic components in the cell will generate the eddy current when spinning in a magnetic field, leading to unstable spin. Recently, Freytag et al.<sup>[35]</sup> ingeniously design a cylindrical jelly roll type cell that is placed in the commercial 4mm rotor, which could spin at a speed of 10 kHz with LiCoO<sub>2</sub> cathode and graphite anode. Figure 10h exhibits the assembled cell, in which the active materials are coated on cellulosic substrate in order to decrease the use of metal. The resolution can greatly improve under MAS condition, giving the opportunity to simultaneously monitor cathode and anode.

## 5. Summary and Outlook

During last two decades, ssNMR techniques have shown their unique capability in studying both the bulk and interfacial issues in electrochemical energy materials and devices. From three key aspects, that is, electrode/electrolyte materials, electrode/electrolyte interfaces and in situ ssNMR, this review paper summarizes recent advances in the investigation of complex electrochemical processes in Li/Na ion batteries such as local structural evolution of the electrode materials with phase changes, formation of composite SEI with organic/inorganic components and operando tracking of Li/Na deposition/stripping processes, etc. It shows clearly that ssNM is becoming a powerful and indispensable tool to trace and quantify important chemical/physical parameters which greatly determine the electrochemical performance of these battery systems.

We expect that ssNMR and MRI will be widely used and continuously developed in this golden-time for high-performance battery research. For the battery's materials, especially paramagnetic materials, there are a large number of paramagnetic ions and complex interactions to complicate the acquired NMR spectra. It is hard to precisely differentiate and quantify the various interactions between paramagnetic metal-ions and target diffusing atoms such as Li<sup>+</sup> or Na<sup>+</sup> and oxygen anions in the lattice framework experimentally. Therefore, it will be beneficial to quantify reaction intermediates and final product in the solid electrochemical reactions via efficient theoretical calculation/simulation, for example, the computation methods for the several interactions in solid-state materials. Moreover, unlike alkali metal nuclei (<sup>6</sup>Li and <sup>23</sup>Na), which have been widely applied in ssNMR investigations, <sup>17</sup>O nucleus has yet to be fully explored by ssNMR in the field of battery technology although it is one of the most important constituent elements of oxides materials. Therefore, ssNMR research will be further extended to other atomic nuclei that are more difficult to detect and interpret in the recent research, such as <sup>17</sup>O and paramagnetic TM nuclei.<sup>[24]</sup> In order to shorten the acquisition time and improve the sensitivity of the <sup>17</sup>O spectrum, the development of high field DNP methods has made it possible to detect the low sensitive <sup>17</sup>O NMR spectra. In addition, economical and efficient enrichment methods have also been developed for enhancing the sensitivity of <sup>17</sup>O. Recently, <sup>17</sup>O-enriched water as a precursor also shows great potential in preparing <sup>17</sup>O-enriched oxides materials.<sup>[37c]</sup> Besides, O<sup>2-</sup> are often directly connected to TM ions in the cathode materials and the variable interactions between them are expected to make NMR spectrum more complex when the TM ions or O<sup>n-</sup> undergo the charge compensation. Therefore, the accurate structural models of materials and the further development of theoretical calculation methods are the prerequisite for analysis of <sup>17</sup>O NMR spectra. On the other hand, the extraction of the dynamics information from paramagnetic materials is still challenging because of their short T<sub>2</sub> and heterogeneity in local Li/Na environments. The further development of advanced equipment and computational methods is expected to tackle these problems, such as using stronger gradient field, MAS PFG probe and the combining theoretical computational chemistries with VT NMR experiments.

Besides analyzing interface composition, quantifying metal microstructures, and tacking interfacial ionic transport, ssNMR can also handle many interfacial issues in batteries. However,



there are still many challenges to probe SEI in ssNMR: i) Low sensitivity. Since SEI film is a trace interfacial phase, ssNMR is not a highly sensitive technique. To obtain spectra with a reasonably good signal-to-noise ratio, it always takes a long time for data accumulation ( $\approx$ days), which can result in extreme low temporal resolution for in situ experiments. Therefore, how to enhance the detection sensitivity of ssNMR is an important research direction in the future; In this respect, DNP technique should be a very useful technique.<sup>[34]</sup> ii) Low resolution. The chemical shifts of diamagnetic SEI components, normally are all around  $\pm 10$  ppm. Even at high spinning speeds of MAS, their signals are always overlapping and difficult to distinguish. Reasonable peak assignments through multinuclear and multi-dimensional spectra under ultrahigh magnetic field will be very helpful to quantitatively understand SEI components and their evolutions after cycling.

In addition, the (electro)chemical processes within an operating battery are transient, ex situ measurements likely to lose some dynamical information and potentially mislead the understanding of the working and failure mechanisms of battery. In this regard, in situ NMR and MRI techniques are urgently required. However, the broad line-width of NMR signal at static state brings big challenges in obtaining the high-resolution spectra. A recent study reported that the high resolution spectra under in situ state could be obtained through rotating a well-designed in situ battery in a commercial MAS NMR probe, which shows a promising research-direction for the further development of in situ NMR techniques.<sup>[35]</sup> However, the acquisition process of this spinning battery is to charge the battery around specific SOC and then put it into the probe for collection, so it is necessary to further develop the spinning battery and in situ probe to make the acquisition mode changing from “in situ” to “operando” in the future. In addition, the line-width of measured materials also greatly affect the spatial resolution of MRI. For instance, the relative narrow line-width of Li metal signal can achieve the spatial resolution of  $\approx 100$   $\mu$ m at present, while it is challenging for studying cathode materials that usually have very broad line-width at static. Analogously, performing MRI experiment with spinning in situ batteries is the alternative. The future development of higher gradient magnetic field and advanced pulse sequences can also further increase the spatial resolution of MRI technique.

In conclusion, the wealth of ssNMR methods can provide unique insights about composition, structure and their evolutions with atomic selectivity at different time/spatial scales, when exploring the complex and multiple-steps coupled (electro)chemical processes in battery systems. ssNMR techniques and battery technologies have had a great of intersections in the past two decades and the newly-developed NMR methods, such as DNP NMR and MRI techniques with enhanced sensitivity and resolution, would continue to offer powerful tools to explore advanced electrochemical energy materials and devices.

## Acknowledgements

X.L., Z.L., and Y.X. contributed equally to this work. This work was financially supported by National Key Research and Development Program of China (grant no. 2018YFB0905400, 2016YFB0901502),

National Natural Science Foundation of China (grant no. 21935009, 21761132030). R.F. acknowledges the support from the National High Magnetic Field Laboratory which is supported by NSF Cooperative Agreement DMR-1644779 and the State of Florida.

## Conflict of Interest

The authors declare no conflict of interest.

## Keywords

in situ NMR, lithium-ion batteries, sodium-ion batteries, solid electrolyte interfaces, solid-state NMR

Received: August 29, 2020

Revised: January 28, 2021

Published online:

- [1] R. Schmich, R. Wagner, G. Horpel, T. Placke, M. Winter, *Nat. Energy* **2018**, *3*, 267.
- [2] J. B. Goodenough, K. S. Park, *J. Am. Chem. Soc.* **2013**, *135*, 1167.
- [3] N. Yabuuchi, K. Kubota, M. Dahbi, S. Komaba, *Chem. Rev.* **2014**, *114*, 11636.
- [4] S. Randau, D. A. Weber, O. Kotz, R. Koerver, P. Braun, A. Weber, E. Ivers-Tiffée, T. Adermann, J. Kulisch, W. G. Zeier, F. H. Richter, J. Janek, *Nat. Energy* **2020**, *5*, 259.
- [5] Z. L. Gong, Y. Yang, *J. Energy Chem.* **2018**, *27*, 1566.
- [6] a) O. Pecher, J. Carretero-González, K. J. Griffith, C. P. Grey, *Chem. Mater.* **2016**, *29*, 213; b) N. Dupre, C. P. Grey, *Chem. Rev.* **2014**, *104*, 4493.
- [7] G. M. Zhong, J. Y. Bai, P. N. Duchesne, M. J. McDonald, Q. Li, X. Hou, J. A. Tang, Y. Wang, W. G. Zhao, Z. L. Gong, P. Zhang, R. Q. Fu, Y. Yang, *Chem. Mater.* **2015**, *27*, 5736.
- [8] Z. Liu, J. Lee, G. Xiang, H. F. Glass, E. N. Keyzer, S. E. Dutton, C. P. Grey, *Chem. Commun.* **2017**, *53*, 743.
- [9] a) S. Haber, M. Leskes, *Adv. Mater.* **2018**, *30*, 1706496; b) A. Marchetti, J. Chen, Z. Pang, S. Li, D. Ling, F. Deng, X. Kong, *Adv. Mater.* **2017**, *29*, 1605895.
- [10] Y. X. Xiang, G. R. Zheng, G. M. Zhong, D. W. Wang, R. Q. Fu, Y. Yang, *Solid State Ionics* **2018**, *318*, 19.
- [11] Y. X. Xiang, X. Li, Y. Q. Cheng, X. L. Sun, Y. Yang, *Mater. Today* **2020**, *36*, 139.
- [12] J. Z. Hu, N. R. Jaegers, M. Y. Hu, K. T. Mueller, *J. Phys. Condens. Matter* **2018**, *30*, 463001.
- [13] E. Umeshbabu, B. Zheng, Y. Yang, *Electrochem. Energy Rev.* **2019**, *2*, 199.
- [14] B. Z. Zheng, X. S. Liu, J. P. Zhu, J. Zhao, G. M. Zhong, Y. X. Xiang, H. C. Wang, W. M. Zhao, E. Umeshbabu, Q. H. Wu, J. Y. Huang, Y. Yang, *Nano Energy* **2020**, *67*, 104252.
- [15] D. W. Wang, G. M. Zhong, W. K. Pang, Z. P. Guo, Y. X. Li, M. J. McDonald, R. Q. Fu, J. X. Mi, Y. Yang, *Chem. Mater.* **2015**, *27*, 6650.
- [16] I. Hung, L. Zhou, F. Pourpoint, C. P. Grey, Z. Gan, *J. Am. Chem. Soc.* **2012**, *134*, 1898.
- [17] W. S. Yoon, C. P. Grey, M. Balasubramanian, X. Q. Yang, D. A. Fischer, J. McBreen, *Electrochem. Solid-State Lett.* **2004**, *7*, A53.
- [18] D. Zeng, J. Cabana, J. Bréger, W. S. Yoon, C. P. Grey, *Chem. Mater.* **2007**, *19*, 6277.
- [19] S. Y. Zheng, G. M. Zhong, M. J. McDonald, Z. L. Gong, R. Liu, W. Wen, C. Yang, Y. Yang, *J. Mater. Chem. A* **2016**, *4*, 9054.

- [20] R. J. Clément, J. Xu, D. S. Middlemiss, J. Alvarado, C. Ma, Y. S. Meng, C. P. Grey, *J. Mater. Chem. A* **2017**, *5*, 4129.
- [21] I. D. Seymour, D. S. Middlemiss, D. M. Halat, N. M. Trease, A. J. Pell, C. P. Grey, *J. Am. Chem. Soc.* **2016**, *138*, 9405.
- [22] W. Zuo, J. Qiu, X. Liu, F. Ren, H. Liu, H. He, C. Luo, J. Li, G. F. Ortiz, H. Duan, J. Liu, M. S. Wang, Y. Li, R. Fu, Y. Yang, *Nat. Commun.* **2020**, *11*, 3544.
- [23] K. Zhou, S. Y. Zheng, F. C. Ren, J. Wu, H. D. Liu, M. Z. Luo, X. S. Liu, Y. X. Xiang, C. Y. Zhang, W. L. Yang, L. H. He, Y. Yang, *Energy Storage Mater.* **2020**, *32*, 234.
- [24] P. J. Reeves, I. D. Seymour, K. J. Griffith, C. P. Grey, *Chem. Mater.* **2019**, *31*, 2814.
- [25] R. A. House, G. J. Rees, M. A. Pérez-Osorio, J.-J. Marie, E. Boivin, A. W. Robertson, A. Nag, M. Garcia-Fernandez, K.-J. Zhou, P. G. Bruce, *Nat. Energy* **2020**, *5*, 777.
- [26] a) T. Chakrabarty, N. Goldin, A. Feintuch, L. Houben, M. Leskes, *ChemPhysChem* **2018**, *19*, 2139; b) S. Bjorgvinsdottir, P. Moutzouri, P. Berruyer, M. A. Hope, L. Emsley, *J. Phys. Chem. C* **2020**, *124*, 16524; c) T. Wolf, S. Kumar, H. Singh, T. Chakrabarty, F. Aussenac, A. I. Frenkel, D. T. Major, M. Leskes, *J. Am. Chem. Soc.* **2019**, *141*, 451.
- [27] J. Wu, X. Zhang, S. Zheng, H. Liu, J. Wu, R. Fu, Y. Li, Y. Xiang, R. Liu, W. Zuo, Z. Cui, Q. Wu, S. Wu, Z. Chen, P. Liu, W. Yang, Y. Yang, *ACS Appl. Mater. Interfaces* **2020**, *12*, 7277.
- [28] a) L. Zhou, M. Leskes, T. Liu, C. P. Grey, *Angew. Chem. Int. Ed. Engl.* **2015**, *54*, 14782; b) C. Yu, S. Ganapathy, E. Eck, H. Wang, S. Basak, Z. Li, M. Wagemaker, *Nat. Commun.* **2017**, *8*, 1086.
- [29] K. Marker, P. J. Reeves, C. Xu, K. J. Griffith, C. P. Grey, *Chem. Mater.* **2019**, *31*, 2545.
- [30] W. Zhao, G. Zhong, M. J. McDonald, Z. Gong, R. Liu, J. Bai, C. Yang, S. Li, W. Zhao, H. Wang, R. Fu, Z. Jiang, Y. Yang, *Nano Energy* **2016**, *27*, 420.
- [31] a) C. Peng, H. Chen, G. Zhong, W. Tang, Y. Xiang, X. Liu, J. Yang, C. Lu, Y. Yang, *Nano Energy* **2019**, *58*, 560; b) X. Liu, W. Zuo, B. Zheng, Y. Xiang, K. Zhou, Z. Xiao, P. Shan, J. Shi, Q. Li, G. Zhong, R. Fu, Y. Yang, *Angew. Chem. Int. Ed.* **2019**, *58*, 18086.
- [32] Y. Xiang, G. Zhong, Z. Liang, Y. Jin, X. Liu, S. Chen, K. Zhou, J. Zhu, M. Lin, H. He, J. Wan, S. Yu, G. Zhong, R. Fu, Y. Li, Y. Yang, *Nat. Nanotechnol.* **2020**, *15*, 883.
- [33] Z. Cheng, M. Liu, S. Ganapathy, C. Li, Z. Li, X. Zhang, P. He, H. Zhou, M. Wagemaker, *Joule* **2020**, *4*, 1311.
- [34] a) M. A. Hope, B. L. D. Rinkel, A. B. Gunnarsdottir, K. Marker, S. Menkin, S. Paul, I. V. Sergeev, C. P. Grey, *Nat. Commun.* **2020**, *11*, 2224; b) Y. Jin, N. H. Kneusels, P. Magusin, G. Kim, E. Castillo-Martinez, L. E. Marbella, R. N. Kerber, D. J. Howe, S. Paul, T. Liu, C. P. Grey, *J. Am. Chem. Soc.* **2017**, *139*, 14992.
- [35] A. I. Freytag, A. D. Pauric, S. A. Krachkovskiy, G. R. Goward, *J. Am. Chem. Soc.* **2019**, *141*, 13758.
- [36] a) H. J. Chang, A. J. Iltott, N. M. Trease, M. Mohammadi, A. Jerschow, C. P. Grey, *J. Am. Chem. Soc.* **2015**, *137*, 15209; b) P. H. Chien, X. Feng, M. Tang, J. T. Rosenberg, S. O'Neill, J. Zheng, S. C. Grant, Y. Y. Hu, *J. Phys. Chem. Lett.* **2018**, *9*, 1990.
- [37] a) M. Ménétrier, I. Saadouné, S. Levasseur, C. Delmas, *J. Mater. Chem.* **1999**, *9*, 1135; b) N. Imanishi, *Solid State Ionics* **1999**, *118*, 121; c) F. Geng, M. Shen, B. Hu, Y. Liu, L. Zeng, B. Hu, *Chem. Commun.* **2019**, *55*, 7550; d) X. Wang, Y. L. Ding, Y. P. Deng, Z. Chen, *Adv. Energy Mater.* **2020**, *10*, 1903864.
- [38] J. J. Wan, J. P. Zhu, Y. X. Xiang, G. M. Zhong, X. S. Liu, Y. X. Li, K. H. L. Zhang, C. Y. Hong, J. M. Zheng, K. Wang, Y. Yang, *J. Energy Chem.* **2021**, *54*, 786.
- [39] a) S. Y. Zheng, C. Y. Hong, X. Y. Guan, Y. X. Xiang, X. S. Liu, G. L. Xu, R. Liu, G. M. Zhong, F. Zheng, Y. X. Li, X. Y. Zhang, Y. Ren, Z. H. Chen, K. Amine, Y. Yang, *J. Power Sources* **2019**, *412*, 336; b) A. Grenier, P. J. Reeves, H. Liu, I. D. Seymour, K. Marker, K. M. Wiaderek, P. J. Chupas, C. P. Grey, K. W. Chapman, *J. Am. Chem. Soc.* **2020**, *142*, 7001.
- [40] C. Peng, G.-H. Ning, J. Su, G. Zhong, W. Tang, B. Tian, C. Su, D. Yu, L. Zu, J. Yang, M.-F. Ng, Y.-S. Hu, Y. Yang, M. Armand, K. P. Loh, *Nat. Energy* **2017**, *2*, 17074.
- [41] a) M. Tang, S. Zhu, Z. Liu, C. Jjiang, Y. Wu, H. Li, B. Wang, E. Wang, J. Ma, C. Wang, *Chem* **2018**, *4*, 2600; b) K. Amin, Q. Meng, A. Ahmad, M. Cheng, M. Zhang, L. Mao, K. Lu, Z. Wei, *Adv. Mater.* **2018**, *30*, 1703868; c) K. Liu, J. M. Zheng, G. M. Zhong, Y. Yang, *J. Mater. Chem.* **2011**, *21*, 4125.
- [42] a) M. Miroshnikov, H. Wang, N. K. Thangavel, K. Mahankali, S. Satapathy, K. Kato, G. Babu, K. P. Divya, L. M. R. Arava, P. M. Ajayan, G. John, *J. Phys. Chem. C* **2020**, *124*, 17939; b) Z. Luo, L. Liu, J. Ning, K. Lei, Y. Lu, F. Li, J. Chen, *Angew. Chem. Int. Ed. Engl.* **2018**, *57*, 9443; c) A. Hoefling, D. T. Nguyen, P. Partovi-Azar, D. Sebastiani, P. Theato, S.-W. Song, Y. J. Lee, *Chem. Mater.* **2018**, *30*, 2915.
- [43] a) Q. Liu, B. Peng, M. Shen, B. Hu, Q. Chen, *Solid State Ionics* **2014**, *255*, 74; b) L. Wei, Q. Liu, Y. Gao, Y. Yao, B. Hu, Q. Chen, *Macromolecules* **2013**, *46*, 4447.
- [44] a) R. Liu, G. Xu, Q. Li, S. Zheng, G. Zhong, Z. Gong, Y. Li, E. Kruskop, R. Fu, Z. Chen, K. Amine, Y. Yang, *ACS Appl. Mater. Interfaces* **2017**, *9*, 43632; b) M. A. Reddy, H. Euchner, R. Witter, O. Clemens, *J. Mater. Chem. A* **2018**, *6*, 6947.
- [45] a) D. L. Smiley, G. R. Goward, *Chem. Mater.* **2016**, *28*, 7645; b) T. Broux, T. Bamine, F. Fauth, L. Simonelli, W. Olszewski, C. Marini, M. Ménétrier, D. Carlier, C. Masquelier, L. Croguennec, *Chem. Mater.* **2016**, *28*, 7683; c) Z. Liu, Y.-Y. Hu, M. T. Dunstan, H. Huo, X. Hao, H. Zou, G. Zhong, Y. Yang, C. P. Grey, *Chem. Mater.* **2014**, *26*, 2513; d) Z. Gao, H. Sun, L. Fu, F. Ye, Y. Zhang, W. Luo, Y. Huang, *Adv. Mater.* **2018**, *30*, 1705702; e) Q. Li, Z. Liu, L. Zheng, R. Liu, J. Lee, G. L. Xu, G. Zhong, X. Hou, R. Fu, Z. Hai, K. Amine, J. Mi, Z. Liu, S. Wu, C. P. Grey, Y. Yang, *Angew. Chem. Int. Ed.* **2018**, *57*, 11918.
- [46] G. Oyama, O. Pecher, K. J. Griffith, S. Nishimura, R. Pigliapochi, C. P. Grey, A. Yamada, *Chem. Mater.* **2016**, *28*, 5321.
- [47] a) G. L. Xu, R. Amine, A. Abouimrane, H. Y. Che, M. Dahbi, Z. F. Ma, I. Saadouné, J. Alami, W. L. Mattis, F. Pan, Z. H. Chen, K. Amine, *Adv. Energy Mater.* **2018**, *8*, 1702403; b) P. K. Nayak, L. Yang, W. Brehm, P. Adelhelm, *Angew. Chem. Int. Ed.* **2018**, *57*, 102.
- [48] L. Yang, X. Li, X. Ma, S. Xiong, P. Liu, Y. Tang, S. Cheng, Y.-Y. Hu, M. Liu, H. Chen, *J. Power Sources* **2018**, *381*, 171.
- [49] a) W. Zuo, J. Qiu, X. Liu, B. Zheng, Y. Zhao, J. Li, H. He, K. Zhou, Z. Xiao, Q. Li, G. F. Ortiz, Y. Yang, *Energy Storage Mater.* **2020**, *26*, 503; b) X. Wu, G. L. Xu, G. Zhong, Z. Gong, M. J. McDonald, S. Zheng, R. Fu, Z. Chen, K. Amine, Y. Yang, *ACS Appl. Mater. Interfaces* **2016**, *8*, 22227.
- [50] R. J. Clement, J. Billaud, A. R. Armstrong, G. Singh, T. Rojo, P. G. Bruce, C. P. Grey, *Energ. Environ. Sci.* **2016**, *9*, 3240.
- [51] X. S. Liu, G. M. Zhong, Z. M. Xiao, B. Z. Zheng, W. H. Zuo, K. Zhou, H. D. Liu, Z. T. Liang, Y. X. Xiang, Z. R. Chen, G. F. Ortiz, R. Q. Fu, Y. Yang, *Nano Energy* **2020**, *76*, 104997.
- [52] J. Conard, H. Estrade, *Mater. Sci. Eng.* **1977**, *31*, 173.
- [53] Y. Mori, T. Iriyama, T. Hashimoto, S. Yamazaki, F. Kawakami, H. Shiroki, *J. Power Sources* **1995**, *56*, 205.
- [54] H. Fujimoto, A. Mabuchi, K. Tokumitsu, N. Chinnasamy, T. Kasuh, *J. Power Sources* **2011**, *196*, 1365.
- [55] N. Leifer, M. F. Greenstein, A. Mor, D. Aurbach, G. Goobes, *J. Phys. Chem. C* **2018**, *122*, 21172.
- [56] J. M. Stratford, P. K. Allan, O. Pecher, P. A. Chater, C. P. Grey, *Chem. Commun.* **2016**, *52*, 12430.
- [57] B. Key, R. Bhattacharyya, M. Morcrette, V. Seznec, J. M. Tarascon, C. P. Grey, *J. Am. Chem. Soc.* **2009**, *131*, 9239.
- [58] W. Tang, Y. Liu, C. Peng, M. Y. Hu, X. Deng, M. Lin, J. Z. Hu, K. P. Loh, *J. Am. Chem. Soc.* **2015**, *137*, 2600.
- [59] K. Kitada, O. Pecher, P. Magusin, M. F. Groh, R. S. Weatherup, C. P. Grey, *J. Am. Chem. Soc.* **2019**, *141*, 7014.

- [60] M. H. Levitt, John Wiley & Sons, Hoboken, NJ **2013**.
- [61] a) A. Mondal, M. Kaupp, *J. Phys. Chem. Lett.* **2018**, *9*, 1480; b) R. Pigliapochi, A. J. Pell, I. D. Seymour, C. P. Grey, D. Ceresoli, M. Kaupp, *Phys. Rev. B* **2017**, *95*, 054412; c) A. Mondal, M. Kaupp, *J. Phys. Chem. C* **2019**, *123*, 8387.
- [62] A. J. Pell, G. Pintacuda, C. P. Grey, *Prog. Nucl. Magn. Reson. Spectrosc.* **2019**, *111*, 1.
- [63] K. Jongsik, S. M. Derek, A. C. Natasha, Y. X. Z. Ben, M. Christian, P. G. Clare, *J. Am. Chem. Soc.* **2010**, *132*, 16825.
- [64] Y. S. Zhang, A. Castets, D. Carlier, M. Menetrier, F. Boucher, *J. Phys. Chem. C* **2012**, *116*, 17393.
- [65] K. Xu, *Chem. Rev.* **2014**, *114*, 11503.
- [66] G. R. Zheng, Y. X. Xiang, L. F. Xu, H. Luo, B. L. Wang, Y. Liu, X. Han, W. M. Zhao, S. J. Chen, H. L. Chen, Q. B. Zhang, T. Zhu, Y. Yang, *Adv. Energy Mater.* **2018**, *8*, 1801718.
- [67] Q. Li, X. Liu, X. Han, Y. Xiang, G. Zhong, J. Wang, B. Zheng, J. Zhou, Y. Yang, *ACS Appl. Mater. Interfaces* **2019**, *11*, 14066.
- [68] G. R. Zheng, Y. X. Xiang, S. J. Chen, S. Ganapathy, T. W. Verhallen, M. Liu, G. M. Zhong, J. P. Zhu, X. Han, W. W. Wang, W. M. Zhao, M. Wagemaker, Y. Yang, *Energy Storage Mater.* **2020**, *29*, 377.
- [69] C. Wan, S. Xu, M. Y. Hu, R. Cao, J. Qian, Z. Qin, J. Liu, K. T. Mueller, J. G. Zhang, J. Z. Hu, *ACS Appl. Mater. Interfaces* **2017**, *9*, 14741.
- [70] J. F. Qian, B. D. Adams, J. M. Zheng, W. Xu, W. A. Henderson, J. Wang, M. E. Bowden, S. C. Xu, J. Z. Hu, J. G. Zhang, *Adv. Funct. Mater.* **2016**, *26*, 7094.
- [71] M. Leskes, G. Kim, T. Liu, A. L. Michan, F. Aussenac, P. Dorffer, S. Paul, C. P. Grey, *J. Phys. Chem. Lett.* **2017**, *8*, 1078.
- [72] J. P. Zhu, J. Zhao, Y. X. Xiang, M. Lin, H. C. Wang, B. Z. Zheng, H. J. He, Q. H. Wu, J. Y. Huang, Y. Yang, *Chem. Mater.* **2020**, *32*, 4998.
- [73] a) C. Fang, J. Li, M. Zhang, Y. Zhang, F. Yang, J. Z. Lee, M. H. Lee, J. Alvarado, M. A. Schroeder, Y. Yang, B. Lu, N. Williams, M. Ceja, L. Yang, M. Cai, J. Gu, K. Xu, X. Wang, Y. S. Meng, *Nature* **2019**, *572*, 511; b) M. J. Zachman, Z. Tu, S. Choudhury, L. A. Archer, L. F. Kourkoutis, *Nature* **2018**, *560*, 345.
- [74] Y. Y. Hu, Z. Liu, K. W. Nam, O. J. Borkiewicz, J. Cheng, X. Hua, M. T. Dunstan, X. Yu, K. M. Wiaderek, L. S. Du, K. W. Chapman, P. J. Chupas, X. Q. Yang, C. P. Grey, *Nat. Mater.* **2013**, *12*, 1130.
- [75] H. Lee, S. Chen, X. Ren, A. Martinez, V. Shutthanandan, M. Vijayakumar, K. S. Han, Q. Li, J. Liu, W. Xu, J. G. Zhang, *ChemSusChem* **2018**, *11*, 3821.
- [76] S. Chen, Y. Xiang, G. Zheng, Y. Liao, F. Ren, Y. Zheng, H. He, B. Zheng, X. Liu, N. Xu, M. Luo, J. Zheng, Y. Yang, *ACS Appl. Mater. Interfaces* **2020**, *12*, 27794.
- [77] A. J. Illott, A. Jerschow, *J. Phys. Chem. C* **2018**, *122*, 12598.
- [78] A. B. Gunnarsdottir, S. Vema, S. Menkin, L. E. Marbella, C. P. Grey, *J. Mater. Chem. A* **2020**, *8*, 14975.
- [79] F. Blanc, M. Leskes, C. P. Grey, *Acc. Chem. Res.* **2013**, *46*, 1952.
- [80] J. Xiao, J. Z. Hu, H. Chen, M. Vijayakumar, J. Zheng, H. Pan, E. D. Walter, M. Hu, X. Deng, J. Feng, B. Y. Liaw, M. Gu, Z. D. Deng, D. Lu, S. Xu, C. Wang, J. Liu, *Nano Lett.* **2015**, *15*, 3309.
- [81] R. E. Gerald, C. S. Johnson, J. W. Rathke, R. J. Klingler, G. Sandí, L. G. Scanlon, *J. Power Sources* **2000**, *89*, 237.
- [82] R. Bhattacharyya, B. Key, H. Chen, A. S. Best, A. F. Hollenkamp, C. P. Grey, *Nat. Mater.* **2010**, *9*, 504.
- [83] P. M. Bayley, N. M. Trease, C. P. Grey, *J. Am. Chem. Soc.* **2016**, *138*, 1955..
- [84] M. Mohammadi, A. Jerschow, *J. Magn. Reson.* **2019**, *308*, 106600.
- [85] M. Klett, M. Giesecke, A. Nyman, F. Hallberg, R. W. Lindstrom, G. Lindbergh, I. Furo, *J. Am. Chem. Soc.* **2012**, *134*, 14654.
- [86] M. Tang, V. Sarou-Kanian, P. Melin, J. B. Leriche, M. Menetrier, J. M. Tarascon, M. Deschamps, E. Salager, *Nat. Commun.* **2016**, *7*, 13284.
- [87] S. Chandrashekar, N. M. Trease, H. J. Chang, L. S. Du, C. P. Grey, A. Jerschow, *Nat. Mater.* **2012**, *11*, 311.
- [88] A. J. Illott, M. Mohammadi, C. M. Schauerer, M. J. Ganter, A. Jerschow, *Nat. Commun.* **2018**, *9*, 1776.
- [89] L. Zhou, M. Leskes, A. J. Illott, N. M. Trease, C. P. Grey, *J. Magn. Reson.* **2013**, *234*, 44.
- [90] N. M. Trease, L. Zhou, H. J. Chang, B. Y. Zhu, C. P. Grey, *Solid State Nucl. Magn. Reson.* **2012**, *42*, 62.
- [91] J. Arai, Y. Okada, T. Sugiyama, M. Izuka, K. Gotoh, K. Takeda, *J. Electrochem. Soc.* **2015**, *162*, A952.
- [92] K. Gotoh, T. Yamakami, I. Nishimura, H. Kometani, H. Ando, K. Hashi, T. Shimizu, H. Ishida, *J. Mater. Chem. A* **2020**, *8*, 14472.
- [93] J. Z. Hu, Z. C. Zhao, M. Y. Hu, J. Feng, X. C. Deng, X. L. Chen, W. Xu, J. Liu, J. G. Zhang, *J. Power Sources* **2016**, *304*, 51.
- [94] H. J. Chang, N. M. Trease, A. J. Illott, D. Zeng, L.-S. Du, A. Jerschow, C. P. Grey, *J. Phys. Chem. C* **2015**, *119*, 16443.
- [95] L. E. Marbella, S. Zekoll, J. Kasemchainan, S. P. Emge, P. G. Bruce, C. P. Grey, *Chem. Mater.* **2019**, *31*, 2762.
- [96] Y. Xiang, G. Zhong, M. Tao, Z. Liang, G. Zheng, X. Liu, Y. Jin, M. Armand, J.-G. Zhang, K. Xu, R. Fu, Y. Yang, *ChemRxiv* **2020**, <https://doi.org/10.26434/chemrxiv.12910259.v1>.
- [97] W. Tang, B. M. Goh, M. Y. Hu, C. Wan, B. B. Tian, X. C. Deng, C. X. Peng, M. Lin, J. Z. Hu, K. P. Loh, *J. Phys. Chem. C* **2016**, *120*, 2600.
- [98] A. J. Illott, M. Mohammadi, H. J. Chang, C. P. Grey, A. Jerschow, *Proc. Natl. Acad. Sci. U. S. A.* **2016**, *113*, 10779.
- [99] J. M. Bray, C. L. Doswell, G. E. Pavlovskaya, L. Chen, B. Kishore, H. Au, H. Alptekin, E. Kendrick, M. M. Titirici, T. Meersmann, M. M. Britton, *Nat. Commun.* **2020**, *11*, 2083.
- [100] B. Lee, E. Paek, D. Mitlin, S. W. Lee, *Chem. Rev.* **2019**, *119*, 5416.
- [101] M. Letellier, F. Chevallier, C. Clinard, E. Frackowiak, J.-N. Rouzaud, F. Béguin, M. Morcrette, J.-M. Tarascon, *J. Chem. Phys.* **2003**, *118*, 6038.
- [102] F. Poli, J. S. Kshetrimayum, L. Monconduit, M. Letellier, *Electrochem. Commun.* **2011**, *13*, 1293.
- [103] J. A. Tang, S. Dugar, G. Zhong, N. S. Dalal, J. P. Zheng, Y. Yang, R. Fu, *SciRep* **2013**, *3*, 2596.
- [104] E. Salager, V. Sarou-Kanian, M. Sathiy, M. Tang, J.-B. Leriche, P. Melin, Z. Wang, H. Vezin, C. Bessada, M. Deschamps, J.-M. Tarascon, *Chem. Mater.* **2014**, *26*, 7009.
- [105] S. Wiemers-Meyer, M. Winter, S. Nowak, *Phys. Chem. Chem. Phys.* **2017**, *19*, 4962.
- [106] S. A. Kayser, A. Mester, A. Mertens, P. Jakes, R. A. Eichel, J. Granwehr, *Phys. Chem. Chem. Phys.* **2018**, *20*, 13765.
- [107] M. Letellier, F. Chevallier, M. Morcrette, *Carbon* **2007**, *45*, 1025.





**Xiangsi Liu** received his Bachelor's degree in Nanjing University of Aeronautics and Astronautics in 2017. He is now a Ph.D. candidate in School of Chemistry and Chemical Engineering, Xiamen University supervised by Prof. Yong Yang. His research focuses on understanding the reaction mechanism of LIBs and NIBs by solid-state NMR, and developing high-performance energy storage materials.



**Ziteng Liang** received his Bachelor's degree in chemistry from Xiamen University in 2018. He is now pursuing his Ph.D. degree in Collaborative Innovation Center of Chemistry for Energy Materials in Xiamen University, under the supervision of Prof. Yong Yang. His research is dedicated to the investigation of sulfide-type solid state batteries using solid state NMR techniques.



**Yuxuan Xiang** received his Bachelor's degree in Nanjing University of Aeronautics and Astronautics in 2016. He is now pursuing his Ph.D. in School of Chemistry and Chemical Engineering, Xiamen University supervised by Prof. Yong Yang. His research focuses on the study and application of solid-state NMR and MRI methods in the energy storage system (such as Li and Na ion batteries) and materials.



**Yong Yang** is a distinguished professor in Chemistry in the State Key Lab for Physical Chemistry of Solid Surface at Xiamen University since 1997. He now also serves as Editor for *J Power Sources*, Board Member of International Battery Materials Association (IBA) and International Meeting of Lithium Battery (IMLB). His main research interests are new electrode/electrolyte materials for Li/Na-ion batteries, in situ spectroscopic techniques, and interfacial reaction mechanism study in electrochemical energy storage and conversion system.